JGR Planets

RESEARCH ARTICLE
10.1029/2019JE006212

Re-examination of the Population, Stratigraphy, and Sequence of Mercurian Basins: Implications for Mercury's Early Impact History and Comparison With the Moon

Csilla Orgel[1,2], Caleb I. Fassett[3], Gregory Michael[1], Christian Riedel[1], Carolyn H. van der Bogert[4], and Harald Hiesinger[4]

[1]Institute of Geological Sciences, Freie Universität Berlin, Berlin, Germany, [2]European Space Research and Technology Centre (ESA/ESTEC), Noordwijk, The Netherlands, [3]NASA Marshall Space Flight Center, Huntsville, Alabama, USA, [4]Institut für Planetologie, Westfälische Wilhelms-Universität, Münster, Germany

Key Points:
- We cataloged 94 basins on Mercury, 1.7 times more certain and probable basins than in previous works
- We observe roughly half of the basin record, where basins older than Borealis are completely erased
- Our results are consistent with a single impactor population that bombarded the surface of Mercury

Supporting Information:
- Supporting Information S1

Correspondence to:
C. Orgel,
csilla.orgel@esa.int

Citation:
Orgel, C., Fassett, C. I., Michael, G., Riedel, C., van der Bogert C. H., & Hiesinger, H. (2020). Re-examination of the population, stratigraphy, and sequence of Mercurian basins: Implications for Mercury's early impact history and comparison with the Moon. *Journal of Geophysical Research: Planets*, *125*, e2019JE006212. https://doi.org/10.1029/2019JE006212

Received 19 SEP 2019
Accepted 1 APR 2020
Accepted article online 30 APR 2020

Abstract Mercury has one of the best-preserved impact records in the inner solar system due to the absence of an atmosphere and relatively unmodified ancient surface. However, our knowledge of the early impact record and the nature of the impacting projectiles are far from complete. To get a better understanding of the early impact history, we examined large impact basins ($D \geq 300$ km) on Mercury. Here we cataloged 94 basins, 80 of which we classify as certain or probable, 1.7 times more than previously recognized. We re-evaluate the crater densities of basins using the buffered nonsparseness correction technique, which we successfully applied for the Moon. In contrast with a previous study, we find that basins have a slightly higher $N(300)$ crater density on Mercury than on the Moon, but similar $N(500)$ basin densities. Based on these results and comparison with the Moon, we infer that no more than half of the basin record remains observable and basins older than Borealis have generally been erased from the basin record. Furthermore, we establish the stratigraphic relationships of basins based on $N(25)$ crater frequencies, absolute model ages, and observations of crosscutting relationships. Similarly to our previous study on the Moon, we found no evidence for a change in the size-frequency distribution of the impacting population; thus, our results are consistent with a single impactor population that bombarded Mercury's surface.

1. Introduction

Mercury has one of the best-preserved impact records in the inner solar system due to its relatively ancient surface and the absence of an atmosphere (Neukum et al., 2001; Spudis & Guest, 1988; Strom & Neukum, 1988). The goal of this paper is to reinvestigate basin and crater densities, use these to probe the early impactor population on Mercury, and compare these with the Moon. Although Mercury and the Moon appear similar at first glance, Mercury experienced higher rates of surface modification than the Moon, as a consequence of both volcanism (Byrne et al., 2018; Denevi et al., 2009; Head et al., 2011; Ostrach et al., 2015; Spudis & Guest, 1988; Whitten et al., 2014) and impact-related resurfacing processes (Braden & Robinson, 2013; Chapman et al., 2018; Fassett et al., 2011; Fassett, Head, Baker, et al., 2012; Kreslavsky et al., 2014; Neukum et al., 2001; Spudis & Guest, 1988; Strom & Neukum, 1988; Strom et al., 2011). The earliest geological mapping (Trask & Guest, 1975) of the planet revealed a variety of important differences compared to the Moon, regarding both the impact basin ($D \geq 300$ km, where D is the basin diameter) and general cratering records, and its extensive volcanic plains.

Fassett, Head, Baker, et al. (2012) cataloged and characterized the basin population ($D \geq 300$ km) on Mercury using data obtained by the MErcury Surface Space ENvironment, Geochemistry, and Ranging (MESSENGER) spacecraft early in its orbital mission and found 46 impact basins, which were classified into three groups: certain (20) and probable (26), as well as a 41 tentative. Many of these tentative basins were proposed based on Mariner 10 and telescopic observation images but could not be verified with the new MESSENGER data.

The nature and history of large impact basin formation on Mercury have been interpreted from two different viewpoints. The first is that the population of basins record a surge or increase in the impact rate during

the early history of the solar system, often called the Late Heavy Bombardment (LHB) (Bottke et al., 2012; Fassett, Head, Kadish, et al., 2012; Head et al., 2010; Marchi et al., 2012, 2013; Morbidelli et al., 2012; Stöffler & Ryder, 2001; Strom et al., 2005, 2015; Tera, 1974). This increase is usually suggested to occur between ~3.8 and 4.1 Gyr based on the dating of lunar samples (Stöffler & Ryder, 2001; Stöffler et al., 2006; Tera, 1974), though the intensity of the postulated change in the impact flux varies substantially between different workers. It has also been proposed that the LHB included impacts from an impactor population that was distinct from the later one, which would be revealed in a crater size-frequency distribution (CSFD), or production function (PF) that changed over time. Such a hypothesis was made based on an observed difference between the CSFDs of the oldest lunar and Mercurian surfaces and younger surfaces (Fassett, Head, Kadish, et al., 2012; Head et al., 2010; Strom et al., 2005, 2011, 2015). Strom et al. (2005, 2011, 2015) investigated the crater populations on the terrestrial bodies and proposed two different impactor populations: Population 1 and Population 2. They proposed that Population 1 impactors from the Main Asteroid Belt formed the oldest, heavily cratered surfaces on Mercury, Moon, and Mars during the LHB. They predicted that LHB began sometime before ~3.9 Gyr and lasted ~100 to 300 Myr. Subsequently, near-Earth objects dominated the Population 2 impactors that cratered younger lightly cratered terrains after 3.8–3.7 Gyr. Based on the CSFDs, they argued that a transition in impactor populations occurred between 3.9 and 3.8 Gyr.

These results were supported by a later CSFD study by Head et al. (2010). Head et al. (2010) determined two different populations of impactors with a transition during the Imbrian period at less than 3.9 Gyr, close to the formation time of the Orientale basin. Their conclusions were mainly based on the premare and postmare crater populations. In contrast to the study conducted by Head et al. (2010), Fassett, Head, Kadish, et al. (2012) normalized and summed the CSFDs of 30 key lunar basins assigned to the same chronostratigraphic period. Their results show a change in impactor population prior to the mid-Nectarian period, which would be consistent with an uptick of the cratering rate at 4.1 Gyr derived by Morbidelli et al. (2012).

The second view is that the basin population formed from an exponentially declining flux of planetesimals or planetesimal-derived debris following planetary accretion or an accretion tail scenario (Baldwin, 2006; Hartmann, 1995; Ivanov, 2008; Morbidelli et al., 2018; Neukum, 1983; Neukum & Ivanov, 1994; Werner, 2014; Zellner, 2017). This scenario involves a collisionally evolved impactor population, contributing to the cratering record within the inner solar system, where the crater PF remained unchanged over time (Neukum, 1983; Orgel et al., 2018). Indeed, Orgel et al. (2018) showed that the apparent difference in the shape of the CSFD of the oldest lunar surfaces in comparison to the younger surfaces could be explained by the incomplete accounting for the smallest craters on heavily or nonsparsely cratered old surfaces. A nonsparse crater population causes the incremental obliteration of the smaller diameter craters in heavily cratered regions. A new technique to account for nonsparseness (Kneissl et al., 2016; Riedel et al., 2018) allowed Orgel et al. (2018) to re-examine the lunar data and correct for the effect.

Correct measurement, fitting, and interpretation of CSFDs on planetary bodies are critical for understanding the geological evolution of planetary surfaces. While the relative frequencies of craters can be used to establish relative ages for geological units, this information can also be converted to absolute model ages (AMAs) using a chronology function (CF), as established for the Moon from the radioisotope and exposure ages of lunar samples (Arvidson et al., 1978; Baldwin, 1971; Neukum, 1971, 1977, 1983; Neukum et al., 2001). This lunar cratering chronology can be extended for use on other planetary bodies by considering parameters such as the body's surface gravity, material properties, and impact velocity (Neukum et al., 2001). Alternatively, Le Feuvre and Wieczorek (2008, 2011) and Marchi et al. (2011) calculate PFs and CFs from a combination of astronomical observations of probable impactors and dynamical calculations to estimate the impact rate. However, due to the lack of Mercurian samples, all current CFs for Mercury have substantial systematic uncertainty, which is then manifested in AMAs on Mercury.

Here, we re-examine the population of basins on Mercury as well as their superposed impact crater populations, as we also did for the Moon (Orgel et al., 2018). From this work, we re-examine the shape and nature of the PF on Mercury, which is critical for understanding early solar system dynamics as well as to estimate AMAs for these major geological events on Mercury. To analyze the superposed impact crater populations, we use the buffered nonsparseness correction (BNSC) (Kneissl et al., 2016; Orgel et al., 2018; Riedel et al., 2018) and the buffered crater counting (BCC) (Fassett & Head, 2008; Fassett, Head, Kadish,

et al., 2012) techniques. We also revisit the stratigraphic relationships of the basins based on crater densities and superposition observations. As part of this process, we establish a new basin catalog for Mercury. This list will serve as a useful basis for targeting for the upcoming BepiColombo mission.

2. Background

Observations from MESSENGER spacecraft data have enabled global re-examination of the cratering record of Mercury and characterization of its crater population for the first time. The new observations show a deficit in crater density in the crater diameter range of 20–128 km in heavily cratered terrains in comparison with the lunar highlands (Fassett et al., 2011; Strom et al., 2011; Strom & Neukum, 1988). However, the density of craters larger than 100 km is similar to the Moon. This may result from global resurfacing processes related to heavy bombardment and volcanism, where smaller craters are easily removed (Fassett et al., 2011; Marchi et al., 2013). Despite the fact that crater formation rates on Mercury are approximately 3 times higher than on the Moon for a given size. Consequently, the observed large craters and basins from the same impactor size-frequency distribution (SFD) are larger on Mercury than on the Moon (Le Feuvre & Wieczorek, 2011; Fassett et al., 2011; Marchi et al., 2011; Strom et al., 2011; Strom et al., 2015).

Baker et al. (2011) and Baker and Head (2013) cataloged complex craters, protobasins, and peak-ring basins ($D \geq 50$ km) on Mercury and the Moon. Their findings for Mercury compared with the Moon were (1) the number of peak-ring basins and protobasins per unit area is higher, (2) the onset diameter of peak-ring basins is smaller, (3) the diameters of complex craters and peak-ring basins overlap more, and (4) complex craters are shallower. Moreover, clear multiring basins are absent on Mercury, which may be explained by (1) lithospheric relaxation, (2) postimpact volcanic resurfacing, or (3) failure to form multiring structures (Fassett, Head, Baker, et al., 2012; Chapman et al., 2018).

Generally, Mercurian basins are morphologically more degraded than the lunar basins and are commonly filled or partially filled with smooth plains. This is consistent with a more extended surface modification by volcanism and higher impact melt production (Baker & Head, 2013; Denevi et al., 2009; Ernst et al., 2015; Ostrach et al., 2012; Whitten & Head, 2015). Other surface degradation and obliteration processes may also play a role (e.g., Fassett et al., 2017), including the more abundant secondary craters on Mercury (Strom, 1977).

Mercurian basin margins are often outlined by tectonic features such as wrinkle ridges, high-relief ridges, and lobate scarps (Byrne et al., 2014, 2018; Strom et al., 1975); these help make the identification of basins easier. The origin of these compressional landforms (thrust-faults and/or folds) has generally been interpreted to be a result of global contraction of the planet. Often, these features postdate the volcanic plains and some of these landforms follow and verge the basin perimeter (Fegan et al., 2017).

It is currently thought that major effusive volcanic activity started on Mercury earlier than 4.1 Gyr and ceased around 3.5 Gyr (Byrne et al., 2016; Head et al., 2011; Ostrach et al., 2015), but the AMAs are highly model dependent. However, small regions of plains and explosive pyroclastic deposits could be as young as few hundred million years old (Denevi, Ernst, et al., 2018; Prockter et al., 2010; Thomas et al., 2014). The oldest interpreted volcanic units are the intercrater plains, which have a rough texture as well as high density of primary and secondary craters ($D < 15$ km) (Denevi, Ernst, et al., 2018; Denevi, Ernst, Whitten, et al., 2013; Head et al., 2009; Oberbeck et al., 1977; Spudis & Guest, 1988; Strom, 1977; Weider et al., 2015; Whitten et al., 2014; Wilhelms et al., 1976). The oldest and most heavily cratered intercrater terrains on Mercury have been estimated to be about 4.0–4.1 Gyr old (Marchi et al., 2013). Younger smooth plains exhibit a sparsely cratered surface covering 25% of the planet with a thickness between 0.5 and 4 km (Denevi et al., 2009; Denevi, Ernst, et al., 2018; Denevi, Ernst, Meyer, et al., 2013; Ernst et al., 2015; Head et al., 2009, 2011; Ostrach et al., 2015; Prockter et al., 2010; Trask & Guest, 1975; Whitten & Head, 2015). Smooth plains are often geographically coincident with impact basins (Caloris, Rembrandt, and numerous other basins in the northern and southern hemispheres); however, the northern smooth plains, which represent 9% of the surface, are not related to any clear large basin (Head et al., 2011). One explanation for the frequent relationship between smooth plains and basins is that large basin-scale impacts may have triggered mantle upwelling and enhanced the production of partial melt in the mantle, even some time after the impact event (Elkins-Tanton & Hager, 2005; Roberts & Barnouin, 2012).

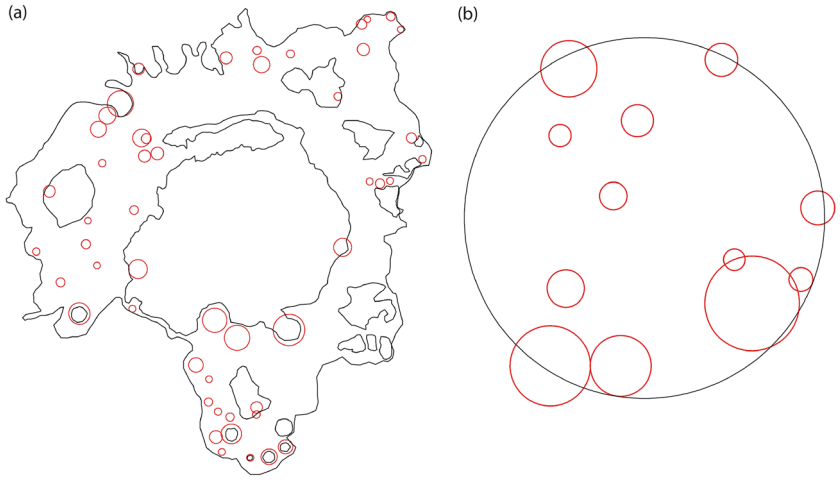

Figure 1. Different mapping approaches for the crater measurements. (a) Craters (red circles) were counted on basin rim and ejecta deposit remnants (black outline), excluding all areas resurfaced by the smooth plains (e.g., Rembrandt basin). (b) All craters were mapped inside the basin cavity (e.g., b102 basin).

3. Data and Methods

3.1. Data

The primary data for this study are optical images from MESSENGER's Mercury Dual Imaging System (MDIS) (Chabot et al., 2016; Hawkins et al., 2007) with a variety of solar incidence and illumination azimuths mosaicked into a 166m/pixel global data set. Additionally, we used the color and enhanced color 665m/pixel global data set (Denevi et al., 2016; Denevi, Chabot, et al., 2018). Topography data from MESSENGER's MDIS digital elevation model (665 m/pixel) (Becker et al., 2016) and Mercury Laser Altimeter (250 m/pixel) (Cavanaugh et al., 2007) served as the main topographic data sets. All data products are available from the Planetary Data System. The data were analyzed in ESRI ArcGIS 10.3.

We re-examined the basin catalog of Fassett, Head, Baker, et al. (2012), which was based on MESSENGER MDIS and Mercury Laser Altimeter data set. We also revisited previously unverified basins noted in Mariner-10 and telescopic observation studies (Tables 2 and 3). To find potential new basins, we inspected the available data sets at a large range of scales. For the recognition and qualitative analysis of the basins, we visually assessed the completeness of the basin rim, ejecta deposit, topography, and additional associated tectonic features, such as lobate scarps and wrinkle ridges. We classified the basins ($D \geq 300$ km) as "certain" (central interior depression and >75% rim completeness), "probable" (central interior depression and >50% rim completeness), or "tentative" (central interior depression and <30% rim completeness), and these were inspected by several of the coauthors both independently and together. By percentage of rim completeness,

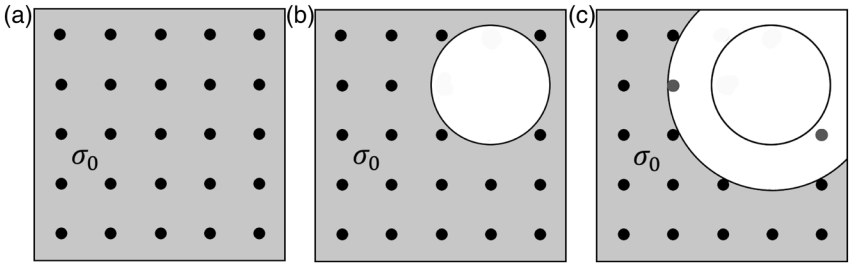

Figure 2. Schematic of nonsparseness correction. (a) The aim is to determine the surface density (σ_0) of small craters. (b) The occurrence of a large crater halfway through the geologic history of the surface diminishes the accumulated population within its boundary. Externally to it, σ_0 remains observable over the gray area. (c) Some region is resurfaced by the large craters' ejecta (one crater radius from the crater rim, craters marked with dark gray circles), the remaining area where σ_0 is measurable is smaller. Note that if we choose the resurfaced area too large, this does not damage our measurement of σ_0 providing sufficient area remains.

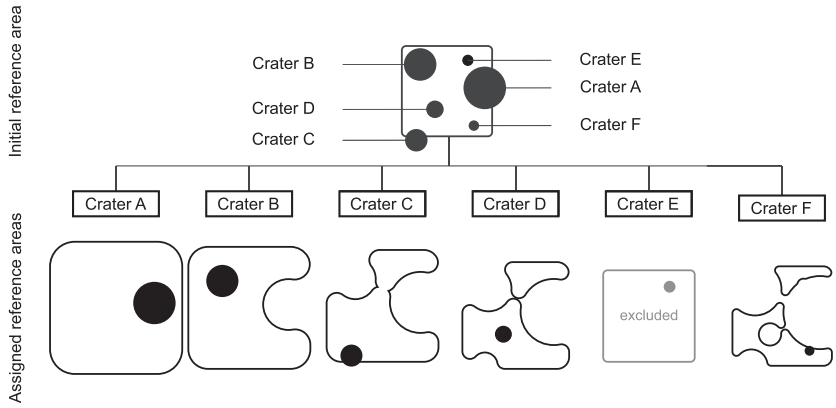

Figure 3. Each crater is assigned to a reference area during buffered nonsparseness correction. In this sketch, there is a rectangular reference area with six differently sized Craters A–F, with Crater A being the largest and Crater F being the smallest crater. Individual craters affect the reference area by one crater radius from the crater rim. Therefore, the affected area by crater obliteration is two times a crater's radius. For every crater under consideration, all larger craters and their surrounding ejecta deposit are discarded from the initial reference area. The remaining area is buffered by one crater radius of the crater, which is currently under examination. If the centroid of the crater is located inside the modified reference area, the investigated crater is included for the analysis. In addition, the reference area for each crater becomes smaller for correspondingly smaller crater sizes. Moreover, in this example, Crater E is excluded since it is located entirely on top of Crater A's ejecta deposit. Consequently, some craters will be excluded during computation. Orgel et al. (2018) have published this figure.

we mean that circular arcs or segments were qualitatively inferred to exist, not necessarily quantitatively measured that a prominent topographic signature of a rim remains. Prominent rim topography is rarely complete on Mercury at basin scales, even for some of the freshest basins. We used both optical and topographic data sets to identify basins; however, the topographic data proved to be the most useful. For consistency, we refer to named basins by the assigned basin names from the International Astronomical Union and the alphanumerical identifiers (e.g., b1, b2, and b3) used by Fassett, Head, Baker, et al. (2012). For the newly discovered basins, we assign new alphanumerical identifiers ≥b69.

3.2. CSFD Measurements

The CraterTools extension in ArcMap (Kneissl et al., 2011) was used to map the CSFDs for basins with diameters ≥25 km. We used two different mapping approaches for the crater measurements: (1) measuring craters on basin rims and ejecta deposits, excluding all areas resurfaced by smooth plains (Figure 1a), and (2) mapping all craters inside the basins' rims, which only provides a lower limit on the accumulated superposed crater population due to resurfacing within the basins (Figure 1b). For calculating the count areas and resulting CSFDs for each basin, we used three different approaches. In the first two approaches, we used the BCC method (Fassett & Head, 2008; Fassett, Head, Kadish, et al., 2012; Kneissl et al., 2015; Tanaka, 1982; Wichman & Schultz, 1989) applied to both mapping approaches, resulting in what we label as BCC1 and BCC2 CSFD measurements (Table 2). In some cases, the first mapping approach was not successful, because the basins are either fully or partially covered by volcanic plains of various thicknesses (e.g., Denevi et al., 2009; Denevi, Ernst, et al., 2018; Fassett, Head, Baker, et al., 2012; Whitten & Head, 2015), so we applied the second mapping approach.

Table 1
Parameters Used for Equations (1) and (2) on the Moon and Mercury

	Moon	Mercury	Reference[b]
v (km/s)	19.4	42.5	1
g (m/s^2)	1.62	3.7	
D_{sg} (km)	0.3	*0.13*	2
D_{sc} (km)	15	11	3 and 4
d (kg/m^3)	2,500	2,500	1
f (kg/m^3)	2,700	2,700	1 and 4
D_p (km)[a]	*1.173*	*1.173*	
D_t (km)[a]	*19.15*	*22.17*	
D (km)[a]	20	*25*	

[a]Calculated values in italics. [b]Source: 1, Le Feuvre and Wieczorek (2008); 2, Neukum and Ivanov (1994); 3, Neukum et al. (2001); and 4, Ivanov (2008).

The BCC technique includes all craters crosscutting the region of interest within a buffer. The buffer in this study is one crater radius radial from the crater rim, which is the region affected by ejecta. Orgel et al. (2018) concluded that different exclusion radii do not significantly change the results. Second, we used a new CSFD measurement approach developed to improve the measurement of the CSFDs of smaller diameter craters on heavily cratered surfaces. This BNSC technique considers and corrects for crater obliteration of smaller diameter craters by larger craters and

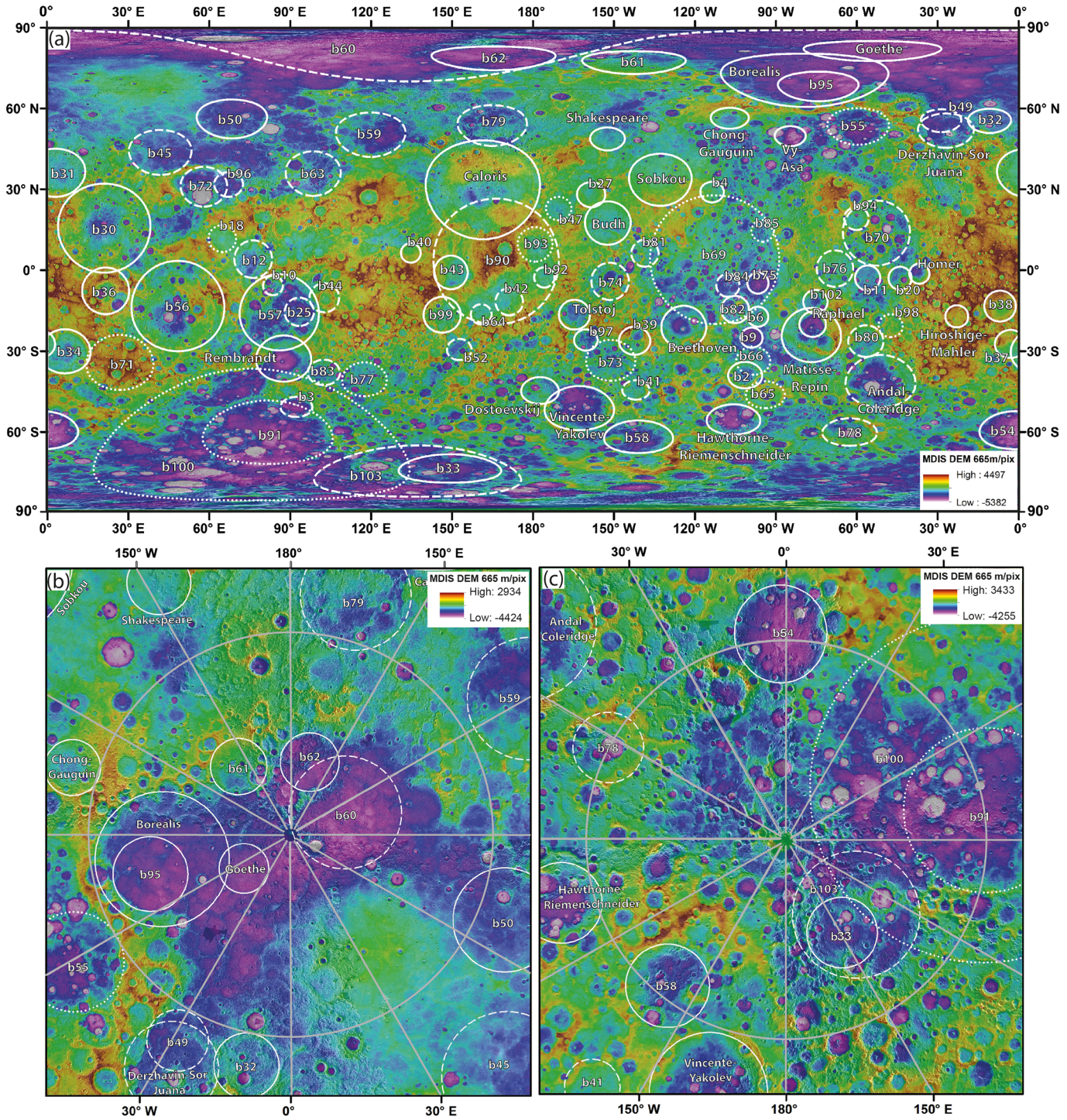

Figure 4. Global distribution of basins on Mercury determined from MESSENGER MDIS 166-m/pix data and MDIS DEM 665m/pix resolution data. The basins were classified as (1) *certain* (solid line), (2) *probable* (dashed line), and (3) *tentative* (dotted line). (a) Global distribution of basins in equidistant cylindrical projection. (b) Polar stereographic projection of the north polar pegion and (c) the south polar region with lines of longitude shown in 30° increments. The reference body is a sphere of 2,440 km in radius.

their ejecta deposits (Kneissl et al., 2016; Orgel et al., 2018; Riedel et al., 2018; Figure 2). Each crater is assigned a buffered reference area that excludes regions that have been modified by subsequent impacts; thus, the reference area becomes smaller for correspondingly smaller crater sizes (Figure 3). Details of the techniques, selection of buffer parameters, and improvements in the resulting data sets can be found in

Journal of Geophysical Research: Planets
10.1029/2019JE006212

Table 2
Certain and Probable Impact Basins on Mercury, D ≥ 300 km

#	Mercury basins	Confidence	*N*(25) BNSC	*N*(25) BCC (1)	*N*(25) BCC (2)	Factor (%)	AMA (Neukum et al., 2001)	AMA (Le Feuvre & Wieczorek, 2011)	Lat. (°)	Lon. (°)	Diameter (km)	Visibility		Stratigraphy[d]	Note[a]
												Topography[b]	Optical data[b]		
1	b42[c]	Probable	745 ± 186	190 ± 42	94 ± 21	292	$\mu 4.09^{+0.1}_{-0.14}$	$\mu 3.87^{+0.027}_{-0.045}$	−11.7	171.1	426	Y	P	> Caloris	c
2	b50	Certain	286 ± 86	112 ± 31	91 ± 15	155	$\mu 4.14^{+0.081}_{-0.10}$	$\mu 3.84^{+0.025}_{-0.029}$	56.1	68.4	615	Y	Y	Undistinguishable relationship with b45	c
3	b96[c]	Probable	195 ± 87	108 ± 32	90 ± 22	81			31.8	67.1	386	Y	P	> Rachmaninoff, b72	d
4	b81	Probable			185 ± 32				6.3	−138.6	425	Y	P	—	d
5	b4	Certain			183 ± 42				29.0	−113.7	322	Y	Y	—	b
6	Borealis[c]	Certain	165 ± 55	104 ± 15	90 ± 10	59	$\mu 4.24^{+0.042}_{-0.059}$	$\mu 3.95^{+0.021}_{-0.031}$	70.5	−79.2	848	Y	Y	> b95, b55, Chong-Gauguin, Vy-Asa, Goethe	b
7	b99	Certain			161 ± 23				−16.5	146.3	562	Y	P	> Caloris	d
8	b61	Certain			160 ± 35				77.1	−142.6	360	Y	Y	Undistinguishable relationship with Borealis	c
9	b64	Probable	158 ± 79	146 ± 73	87 ± 27	8	$\mu 3.99^{+0.11}_{-0.17}$	$\mu 3.80^{+0.044}_{-0.086}$	−16.3	160.8	314	Y	Y	> Caloris, b90	b
10	b84	Probable			155 ± 47				−5.7	−107.8	364	Y	N	undistinguishable relationship with b82, b75	d
11	b25	Probable			153 ± 28				−15.4	93.3	444	Y	N	> Rembrandt, b44	c
12	b97	Certain			151 ± 36				−25.9	−160.4	334	Y	Y	> Tolstoj	d
13	b82	Certain			150 ± 29				−14.5	−105.1	425	Y	P	—	d
14	b63	Probable			149 ± 18				36.3	97.3	700	Y	N	—	c
15	Haworth-Riemenschneider	Certain			142 ± 25				−55.4	−105.7	481	Y	P	—	b
16	b45	Probable	139 ± 35	116 ± 24	76 ± 12	20	$\mu 4.03^{+0.064}_{-0.077}$	$\mu 3.82^{+0.029}_{-0.036}$	43.7	41.8	711	Y	Y	> b72	b
17	Dostoevskij	Certain	136 ± 29	109 ± 21		25	$\mu 3.96^{+0.066}_{-0.80}$	$\mu 3.82^{+0.018}_{-0.020}$	−44.6	−177.5	423	Y	Y	—	a
18	Raphael	Certain	128 ± 32	100 ± 23		28	$\mu 4.01^{+0.036}_{-0.040}$	$\mu 3.77^{+0.022}_{-0.026}$	−20.1	−76.4	394	Y	Y	—	a
19	*Vincent-Yakolev*	Certain			126 ± 17				−50.1	−163.6	699	Y	Y	> Dostoevskij	b
20	b78	Probable			118 ± 25				−60.0	−62.7	431	Y	P	—	d
21	b54	Certain			117 ± 18				−57.2	−0.2	595	Y	N	—	b
22	b52	Probable			116 ± 30				−29.4	152.6	336	P	N	—	b
23	*b58*	Certain			113 ± 21				−61.7	−140.9	513	Y	Y	> Vincent-Yakolev	c
24	b70	Probable			113 ± 11				13.8	−52.8	1,028	Y	P	> b94, b76, b11, b20, Homer	d
25	Hiroshige-Mahler	Certain			112 ± 30				−17.1	−23.0	345	Y	Y	—	b
26	b76	Probable			112 ± 19				0.6	−68.1	577	Y	N	> b11	d
29	b103	Probable			106 ± 13				−74.5	137.2	814	Y	P	> b33	d
30	b31	Certain			104 ± 14				36.2	3.0	758	Y	N	> b30	b
31	b59	Probable			102 ± 15				50.1	119.3	701	Y	N	> Caloris	c
32	*b57*	Certain			100 ± 9				−15.5	85.8	1,203	Y	N	> b44, Rembrandt, b25, b101, b12	c
33	b62	Certain			95 ± 25				78.6	165.3	376	Y	N	> Caloris	c

Journal of Geophysical Research: Planets

10.1029/2019JE006212

Table 2
Continued

#	Mercury basins	Confidence	*N*(25) BNSC	*N*(25) BCC (1)	*N*(25) BCC (2)	Factor (%)	AMA (Neukum et al., 2001)	AMA (Le Feuvre & Wieczorek, 2011)	Lat. (°)	Lon. (°)	Diameter (km)	Visibility		Stratigraphy[d]	Note[a]
												Topography[b]	Optical data[b]		
34	b43	Certain			95 ± 18				−0.8	149.5	531	Y	P	> Caloris	c
35	b92	Probable			94 ± 28				−2.7	−175.8	320	Y	N	—	d
36	*Sobkou*	Certain	92 ± 17	83 ± 13	64 ± 9	11	$\mu 3.99^{+0.029}_{-0.037}$	$\mu 3.77^{+0.018}_{-0.026}$	33.6	−132.9	821	Y	Y	> b4, Budh, b27	a
37	b41	Probable			89 ± 29				−44.4	−141.9	308	P	P	—	b
38	Chong-Gauguin	Certain	88 ± 29	64 ± 21		38	$\mu 4.08^{+0.071}_{-0.086}$	$\mu 3.85^{+0.030}_{-0.037}$	56.4	−107.1	332	Y	Y	Undistinguishable relationship with Vy-Asa	a
39	b94	Probable			87 ± 25				19.2	−60.2	364	Y	N	—	d
40	b101	Probable			86 ± 27				−5.6	83.6	311	Y	P	—	d
41	b74	Probable		86 ± 16					−4.1	−151.5	589	Y	N	> Tolstoj	d
42	Andal-Coleridge	Probable			85 ± 12				−41.1	−51.2	828	Y	P	—	b
43	b33	Certain			84 ± 20				−73.5	149.1	452	Y	Y	—	b
44	Budh	Certain			84 ± 14				17.5	−152.3	687	Y	N	> b27	b
45	b3	Probable			83 ± 27				−50.7	92.3	318	Y	P	—	b
46	b38 (Sanai)	Certain	83 ± 15	66 ± 11		26	$\mu 3.94^{+0.056}_{-0.066}$	$\mu 3.75^{+0.035}_{-0.056}$	−13.3	−6.9	485	Y	Y	—	a
47	b56 (Lennon-Picasso)	Certain			82 ± 7				−13.3	48.4	1,426	Y	N	> b36	c
48	Matisse-Repin[c]	Certain	82 ± 16	64 ± 8		28	$\mu 3.99^{+0.027}_{-0.034}$	$\mu 3.93^{+0.021}_{-0.031}$	−24.0	−76.9	852	Y	Y	> Raphael, b102	a
49	b39	Certain	81 ± 28	81 ± 19		0	$\mu 3.98^{+0.085}_{-0.11}$	$\mu 3.84^{+0.028}_{-0.048}$	−26.1	−142.4	444	Y	Y	> Beethoven	a
50	Tolstoj	Certain	81 ± 17	77 ± 14	77 ± 13	5	$\mu 3.97^{+0.034}_{-0.037}$	$\mu 3.76^{+0.021}_{-0.025}$	−16.5	−164.7	467	Y	Y	—	a
51	b30 (Calder-Hodgkins)	Certain			80 ± 7				15.6	21.0	1,404	Y	P	> b36	b
52	b40	Certain			80 ± 26				6.4	134.7	308	Y	P	> Caloris	b
53	b75	Certain			77 ± 24				−4.8	−96.7	332	Y	N	—	d
54	b95	Certain			74 ± 18				68.2	−74.3	468	Y	N	—	b
55	b11	Certain	73 ± 42	129 ± 49	94 ± 23	−44			−2.9	−56.0	396	Y	Y	> b20	b
56	b12	Probable	73 ± 24	79 ± 19	56 ± 12	−8	$\mu 4.10^{+0.047}_{-0.070}$	$\mu 3.91^{+0.026}_{-0.043}$	4.1	76.3	594	Y	N	Undistinguishable relationship with b18	b
57	b37 (Aneirin)	Certain	71 ± 21	56 ± 16		27	$\mu 4.01^{+0.059}_{-0.069}$	$\mu 3.79^{+0.035}_{-0.049}$	−27.3	−3.0	442	Y	Y	—	a
58	b36	Certain	71 ± 15	53 ± 8		34	$\mu 4.08^{+0.039}_{-0.053}$	$\mu 3.84^{+0.022}_{-0.026}$	−7.6	21.6	737	Y	Y	—	a
59	b80	Probable			69 ± 17				−26.2	−56.7	498	Y	N	> Matisse-Repin, Undistinguishable relationship with Andal-Coleridge	d
60	Homer	Certain	68 ± 19	62 ± 16		10	$\mu 4.02^{+0.054}_{-0.063}$	$\mu 3.80^{+0.031}_{-0.040}$	−1.3	−36.8	318	Y	Y	—	a
61	b79	Probable			68 ± 13				53.7	164.9	645	Y	N	> Caloris	d
64	*b102*	Certain			63 ± 21				−11.7	−75.4	375	Y	P	> Raphael	d
65	*b32*	Certain		55 ± 22	48 ± 12				55.4	−10.8	384	Y	Y	> Derzhavin-Sor Juana	b
66	b44	Probable			51 ± 11				−10.2	102.6	459	Y	N	—	b
67	b34	Certain			51 ± 10				−30.0	6.5	696	Y	P	> b37	b
68	Vy-Asa	Certain	44 ± 18	33 ± 12		33	$\mu 3.96^{+0.052}_{-0.082}$	$\mu 3.82^{+0.050}_{-0.11}$	49.7	−84.7	317	Y	Y	—	a
69	*b20*	Certain	42 ± 21	56 ± 20		−25	$\mu 3.87^{+0.064}_{-0.12}$	$\mu 3.94^{+0.050}_{-0.075}$	−3.0	−44.0	364	Y	P	> Homer	a
70	b72	Probable			42 ± 10				31.0	58.0	629	Y	P	> Rachmaninoff	d

Table 2
Continued

#	Mercury basins	Confidence	$N(25)$ BNSC	$N(25)$ BCC (1)	$N(25)$ BCC (2)	Factor (%)	AMA (Neukum et al., 2001)	AMA (Le Feuvre & Wieczorek, 2011)	Lat. (°)	Lon. (°)	Diameter (km)	Visibility Topography[b]	Visibility Optical data[b]	Stratigraphy[d]	Note[a]
71	Beethoven	Certain	40 ± 9	38 ± 8		5	$\mu 3.85^{+0.053}_{-0.062}$	$\mu 3.70^{+0.034}_{-0.059}$	−21.0	−124.2	661	Y	Y	—	a
72	b2	Certain	40 ± 16	51 ± 17	58 ± 16	−22	$\mu 3.90^{+0.077}_{-0.099}$	$\mu 3.71^{+0.039}_{-0.094}$	−38.9	−101.4	420	Y	Y	—	a
73	Rembrandt	Certain	35 ± 6	36 ± 6		−3	$\mu 3.86^{+0.028}_{-0.035}$	$\mu 3.65^{+0.038}_{-0.15}$	−32.7	87.5	731	Y	Y	—	a
74	Caloris	Certain	35 ± 7	28 ± 7		25	$\mu 3.78^{+0.035}_{-0.047}$	$\mu 3.66^{+0.078}_{-0.50}$	29.9	161.4	1,556	Y	Y	—	a
75	b60	Probable			123 ± 16				80.4	134.3	877	Y	N	> b61, b62	c
76	*b90*	Probable			44 ± 3				3.4	166.3	1,977	Y	N	> Caloris, b99, b64, b42, b43, Tolstoj, b92	d
77	b27	Certain							28.0	−158.5	393	Y	N		a
78	b6	Certain							−17.2	−96.7	312	Y	P	> b82, b9	b
79	b9	Certain							−25.0	−99.0	316	Y	N	—	b
80	b49	Probable							55.5	−28.8	362	Y	P	> Derzhavin-Sor Juana	c

Note. Large Mercurian basins ranked by crater densities using buffered nonsparseness correction (BNSC) and buffered crater counting (BCC), respectively. Discrepancies between $N(25)$ and relative stratigraphy are marked with italics. Six basins (from b60 to b49) at the bottom of Table 2 are out of the sequence due to the paucity of craters or large uncertainty on the crater density measurements (e.g., b90 and b60).
[a]Data are from Fassett, Head, Baker, et al. (2012): (a) certain in Fassett, Head, Baker, et al. (2012), (b) probable in Fassett, Head, Baker, et al. (2012), (c) not verified by Fassett, Head, Baker, et al. (2012), and (d) this study. [b]Visibility of basins, P = Possible, N = No, Y = Yes. [c]Basins might be in saturation equilibrium. [d]X, pre-dates X based on stratigraphy.

Kneissl et al. (2016), Orgel et al. (2018), and Riedel et al. (2018). Thus, we used CSFD_Tools (Riedel et al., 2018) and applied a BNSC in concert with the first mapping approach (29 basins) (Table 2).

3.3. Determination of AMAs

We determined the AMAs of the Mercurian basins using the CraterStats software (Michael, 2013; Michael et al., 2016; Michael & Neukum, 2010) and applied both the PF and CF from Neukum et al. (2001), as well as the Le Feuvre and Wieczorek (2011) nonporous scaling model (Table 2). The Le Feuvre & Wieczorek (2011) nonporous model defines crater production for large craters ($D > 20$ km) formed at depths larger than the given megaregolith thickness. We use the μ notation, which captures the systematic uncertainty in the overall CF used (Michael et al., 2016). We plotted the data in cumulative form using pseudolog crater binning (Arvidson et al., 1978; Neukum, 1983), so that it can be directly compared with similar lunar data sets.

AMAs can be fit to any of the CSFDs that we derived via the BCC and BNSC techniques. However, we present AMAs that are fit to the BNSC-derived CSFDs, because of the improvement in the measurement of crater frequencies in the smaller diameter bins, which allows fitting of ages over a broader diameter range, thus improving the error bars (see, e.g., Riedel et al., 2018; Orgel et al., 2018; see also supporting information). Because of the high uncertainties on AMAs on Mercury, we also ranked the basins based on $N(25)$ derived by the BNSC approach to give the relative stratigraphy of the basins. We also compared this relative stratigraphy with values derived from using the BCC1 and BCC2 approaches (Table 2). As an independent check of our results, we compared the obtained ranking of basins with their observed relative stratigraphic relationships. Note that four basins (b11, b32, b96, and Goethe) cannot be assigned AMAs due to the large scatter of their CSFDs.

3.4. Comparison With Lunar Basins

Orgel et al. (2018) used the AMAs and $N(20)$ values of the lunar basins to rank them in temporal sequence. Each derived $N(20)$ value represents the measured frequency of craters ≥20 km normalized to an area of 10^6 km^2. The error was calculated by dividing the $N(20)$ value by the square root of the number of craters in this population. In order to compare the crater densities of Mercurian basins with the lunar basins, we rescaled the values of $N(20)_{\mathrm{Moon}}$ to $N(\mathrm{X})_{\mathrm{Mercury}}$. In other words, we estimated the size of the impactor that forms an impact crater with the diameter of 20 km on the Moon and calculated the size of the impact crater that would be formed by that same impactor on Mercury. We applied the crater-scaling rule from Schmidt and Housen (1987) in Ivanov et al. (2008):

$$D_t/D_p = 1.21*(d/f)^{0.427}*v^{0.564}/\left[g*\left(D_{sg}+D\right)\right]^{0.282} \quad (1)$$

where D_t is the transient cavity diameter, D_p is the projectile diameter, d and f are target and projectile densities, v is impactor velocity, g is surface gravity, D_{sg} is the diameter strength to gravity transition, and D is the final crater diameter. Note that D_{sg} is calculated from the lunar value presuming an inverse dependence of this

term on gravitational acceleration and the same strength on both bodies. We used the equation from Chapman and McKinnon (1986) to calculate the transient diameter for a complex crater:

$$D_t = {D_{sc}}^{0.15} * D^{0.85} \quad (2)$$

where D_{sc} is the transition diameter from simple to complex crater. All parameters are listed in Table 1. The results allow the comparison of the cumulative number of craters on each body that were formed by similarly sized impactors.

Finally, we derived the shape of the summed CSFDs of Pre-Tolstojan- (>4.0 Gyr, Neukum et al., 2001), and Tolstojan-aged (4.0–3.9 Gyr, Neukum et al., 2001) basins using an R-plot with 10 per decade binning. If Neukum's (1983, 2001) model about an unchanging population of impactors is correct, the CSFDs should fit with the isochrons of the PF represented on the R-plot, if the impactor population changed, the CSFDs should deviate from the Neukum PF.

4. Results

4.1. Updated Basin Inventory on Mercury

Most of the basins on Mercury are buried to variable degrees by thick smooth plains, intercrater plains, or impact melt on the surface of Mercury. In addition, candidate basins are often surrounded by scarps and other tectonic landforms, rather than obvious intact basin rims. Thus, the topographic data are extremely useful for identifying "hidden" basins not seen by earlier studies (Fassett, Head, Baker, et al., 2012; Neukum et al., 2001; Spudis & Guest, 1988).

Altogether, we identified and verified 49 certain, 31 probable (Figure 4 and Table 2), and 14 tentative basins (Figure 4 and Table 3) on the surface of Mercury. This is 1.7 times more certain and probable basins than in the previous study (Fassett, Head, Baker, et al., 2012), which was finished before the topography data used here were available.

1. We discovered 30 new basins (alphanumerical identifiers ≥b69, Table 2) and verified 17 basins from the list of unverified basins from Fassett, Head, Baker, et al. (2012).
2. The remaining 24 on the list of unverified basins from Fassett, Head, Baker, et al. (2012) were not confirmed to exist on topographic data, even though some of them (e.g., Bartok-Ives, Gluck-Holbein, and Tir) have International Astronomical Union approved names.

4.1.1. Examples of Newly Discovered Basins

Here, we present two examples out of 30 newly discovered basins (Figure 5 and Table 2).

4.1.1.1. The 375-km-Diameter Basin (b102) at 11.7°S, 75.4°W

The basin designated as b102 has a diameter of 375 km and was identified and classified as *certain*. It is located north of the Matisse-Repin and Raphael basins, and is centered at −11.7°S, −75.4°W (Figure 5 and supporting information). Based on the $N(25)$ crater frequency using the BCC2 technique (Table 2), the basin belongs to the Tolstojan period, however, stratigraphically it predates Raphael basin, which is a Pre-Tolstojan basin. Thus, the b102 basin must be older than the $N(25)$ value suggests. Smooth plains overprint the basin interior, which commonly exhibits low-reflectance material (Denevi, Ernst, Meyer, et al., 2013; Denevi, Ernst, et al., 2018). The rim of the basin is hardly visible in optical data, but ~50% of the northern part of the rim is apparent topographically. Lobate scarps are localized at the western and northern/eastern basin rims, showing signs of tectonic faulting and folding. The scarp at the western rim shows tectonic faulting away from the basin center, while the eastern and northern scarps face toward the basin center.

4.1.1.2. The 645-km-Diameter Basin (b79) at 53.7°N, 164.8°E

A second example of a newly discovered basin (b79) is a degraded 645 km-diameter feature classified as *probable*. It is located north of the Caloris basin and lies beneath its ejecta (Figure 5 and supporting information). Its geographic setting is analogous to the Mendel-Rydberg basin on the Moon, which is superposed by Orientale. The Caloris ejecta deposit (Odin Formation) that buries b79 is characterized by numerous kilometer-scale hummocky hills (see, e.g., Ackiss et al., 2015; Fassett et al., 2009). The basin rim is only recognizable as wrinkle ridges in topographic data but is arcuate in its northern portion. The basin itself is a distinctive circular low area in the topography data, except where it is directly under the Caloris rim.

Table 3
Tentative Impact Basins on Mercury, D ≥ 300 km

#	Mercury basins	Confidence	Lat. (°)	Lon. (°)	Diameter (km)	Visibility		Stratigraphy[c]	Note[a]
						Topography[b]	Optical data[b]		
1	b18	Tentative	11.8	64.8	424.97	P	P	undistinguishable relationship with b12	c
2	b47	Tentative	22.9	−170.5	370.95	Y	N	> Caloris	c
3	b55	Tentative	53.4	−59.5	579.81	P	N	undistinguishable relationship with Vy-Asa	c
4	b65	Tentative	−46.2	−93.9	425.48	Y	N	> b2,might predate Hawthorne-Riemenschneider	b
5	b66	Tentative	−33.5	−98.4	446.74	Y	N	> b2, b9	c
6	b69	Tentative	4.0	−112.7	2,032.31	Y	N	> b85, b4, Sobkou, b81, Beethoven, b82, b84, b75, b6	d
7	b71	Tentative	−34.1	26.8	872.79	P	N	undistinguishable relationship with b56, > b34	d
8	b73	Tentative	−33.4	−151.3	646.45	Y	P	> b39, b97	d
9	b77	Tentative	−40.5	117.5	537.00	Y	N	Undistinguishable relationship with b83	d
10	b85	Tentative	14.6	−94.9	343.50	Y	N		d
11	b91	Tentative	−60.1	81.7	1,001.09	Y	N	> b3	d
12	b93	Tentative	9.6	−179.3	542.88	Y	N	pre-Caloris	d
13	b98	Tentative	−20.6	−47.5	358.39	Y	P		d
14	b100	Tentative	−61.0	75.7	2,081.86	P	N	> b91, b3, Rembrandt, b83, b77, b54, b33, b103	d

[a]Data are from Fassett, Head, Baker, et al. (2012): (a) certain in Fassett, Head, Baker, et al. (2012), (b) probable in Fassett, Head, Baker, et al. (2012), (c) not verified by Fassett, Head, Baker, et al. (2012), and (d) this study. [b]Visibility of basins, P = Possible, N = No, Y = Yes. [c]>X, pre-dates X based on stratigraphy.

Interestingly, the anomalous low topography created by b79 slightly extends into Caloris itself; similar inheritance of precrater topography is seen elsewhere on the Moon, Mars, and Mercury (Howard, 2007).

4.1.2. Examples of Newly Identified Tentative Basins

Here, we describe two examples out of 14 tentative basins. Of these 14 basins, 9 were newly identified in this study (Table 3). The remaining five basins were already listed as *unverified* in Fassett, Head, Baker, et al. (2012).

4.1.2.1. The 2,032-km-Diameter Basin (b69) at 3.9°N, 112.7°W

A tentative basin (b69) with a diameter of 2,032 km is located beneath the ejecta NW of Sobkou basin at 3.9°N, −112.7°W (Figure 5 and supporting information). If confirmed, b69 stratigraphically predates a number of basins, including b4, b6, b75, b81, b82, b84, b85, Sobkou, and Beethoven. Thus, b69 would be a relatively ancient and much degraded Pre-Tolstojan basin. This location partly overlaps with the Mg-rich region on Mercury, where the existence of a basin has been previously suggested (Weider et al., 2015) but has never been clearly demonstrated on the basis of earlier geological analyses. The main lines of evidence for b69 being a candidate basin are (a) that its interior shows a depression that is approximately circular in outline and (b) that it exhibits a number of lobate scarps that are circumferential to the tentative basin location. The reasons the basin is classified as *tentative* rather than *probable* are that a topographic high is present in the NW quadrant of the proposed location, and the basin rim is not visible in either topography or optical data.

4.1.2.2. The 2,081-km-Diameter Basin (b100) at 60.9°S, 75.7°E

Another example of a tentative basin is a 2,081km-diameter basin (b100) at −60.9°S, 75.7°E) with an uncertain extent, but an interior that is a broad topographic depression (Figure 5 and supporting information). Some of the tectonic landforms in the region are broadly circumferential to the tentative basin location as well. Additionally, b91 could be a possible offset peak ring for b100 as the size of this tentative basin would allow that. If confirmed, b100 predates b3, b33, b54, b77, b83, b91, 103, and Rembrandt, which would mean that it is one of the oldest basins on Mercury.

4.2. Crater Frequencies With BNSC

The surface of Mercury went through extensive modification processes due to volcanic activity, which makes it challenging to measure accumulated crater densities corresponding to older basin surfaces. There is no method to compensate for the destruction of smaller craters on volcanically resurfaced areas. However, the BNSC technique corrects for the geometric obliteration of small craters by larger impacts and their corresponding ejecta deposits, and therefore can better estimate crater densities on surface units, where this form of obliteration dominates crater erasure (Kneissl et al., 2016; Orgel et al., 2018). The BNSC

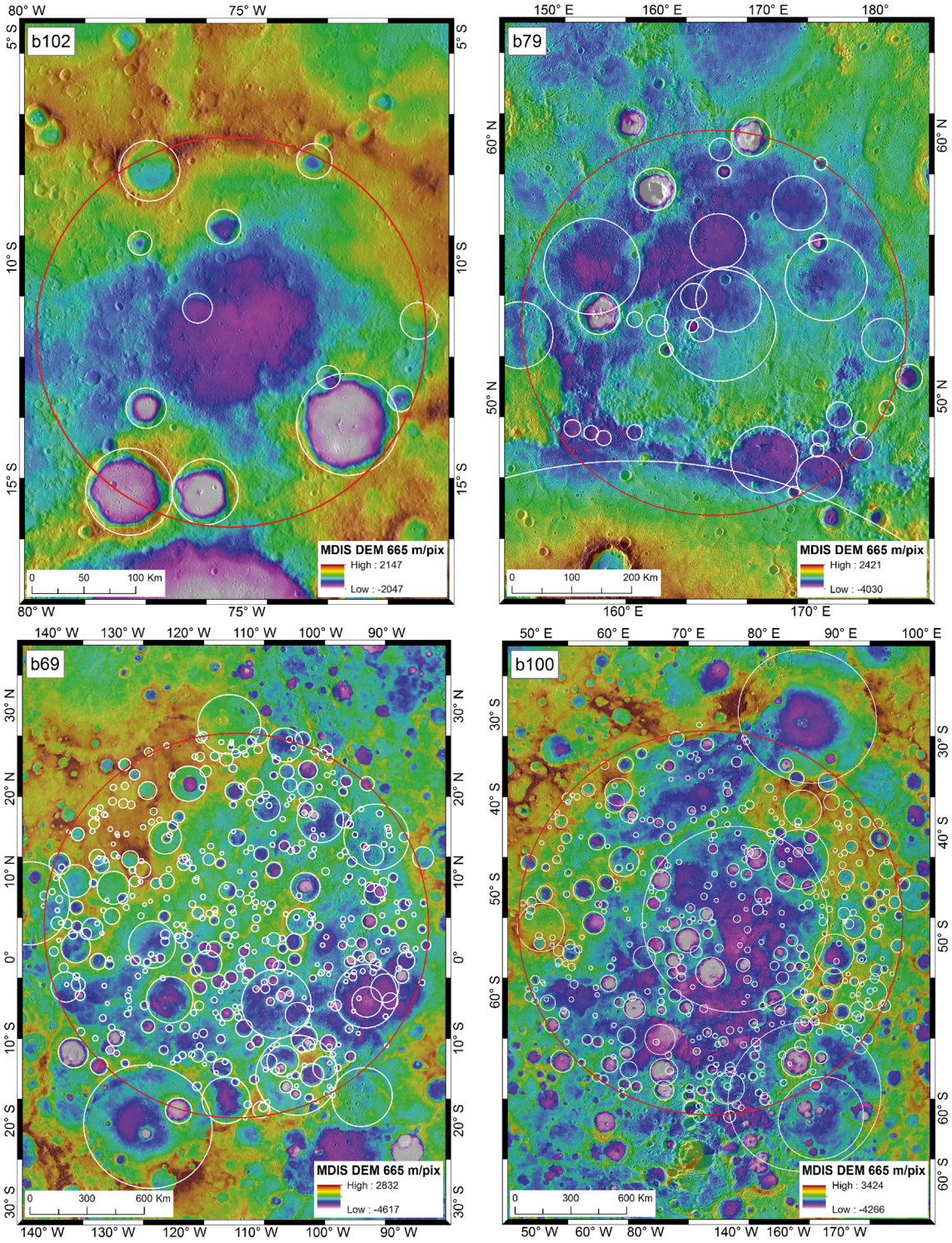

Figure 5. Examples of newly discovered basins overlaid on MDIS DEM 665 m/pix and MDIS monochrome data set. B102 is a *certain* basin with an almost completely preserved rim. B79 is categorized as *probable* and is situated north and beneath Caloris basin. B69 is a *tentative* basin overlapping with the proposed Mg-rich region on Mercury (Weider et al., 2015). B100 is a *tentative* basin covering a large portion of the south polar region on Mercury.

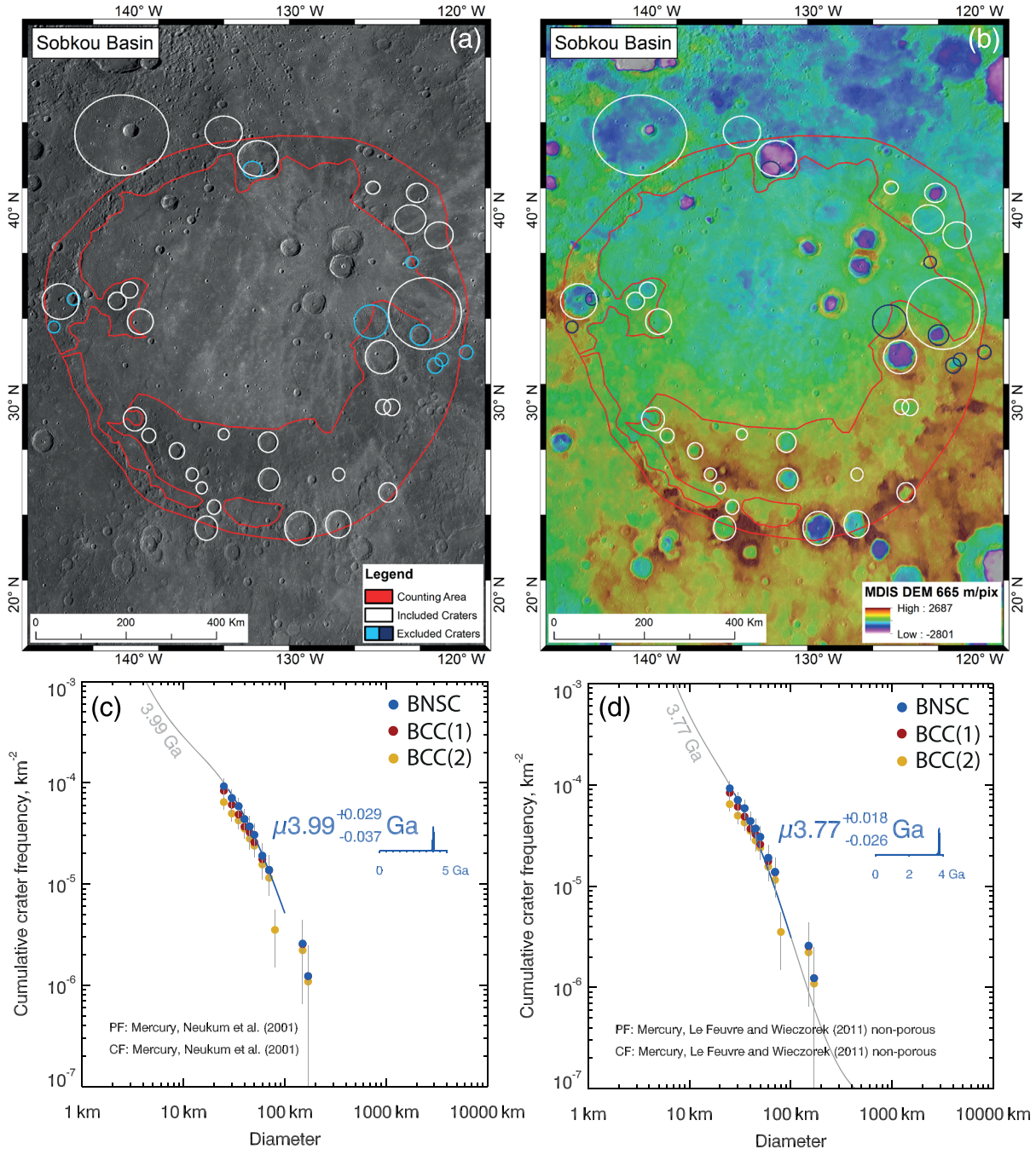

Figure 6. Crater measurement maps and derived CSFD with AMA of Sobkou basin after Neukum et al. (2001) and Le Feuvre and Wieczorek (2011). (a) Counting area on MESSENGER's Mercury Dual Imaging System (MDIS) 166-m/pixel mosaic base map. Craters marked in white were counted for BNSC age determination, whereas craters marked in blue were excluded during computation. We applied one crater radius radial from the crater rim, which removes the region obliterated by the craters and their proximal ejecta. (b) Counting area on MESSENGER's Mercury Dual Imaging System (MDIS) DEM 665m/pixel mosaic base map. Legend for panel (a) is the same as for panel (b). (c, d) Cumulative CSFD plots of Sobkou basin using two different crater counting techniques: BCC (1: red circles, 2: yellow circles) and BNSC (blue circles). The BNSC data show that the smallest crater bins were corrected to higher crater frequencies when accounting for crater nonsparseness. AMAs derived from the Neukum et al. (2001) (c) and Le Feuvre and Wieczorek (2011) chronology functions (d) using Poisson age analysis.

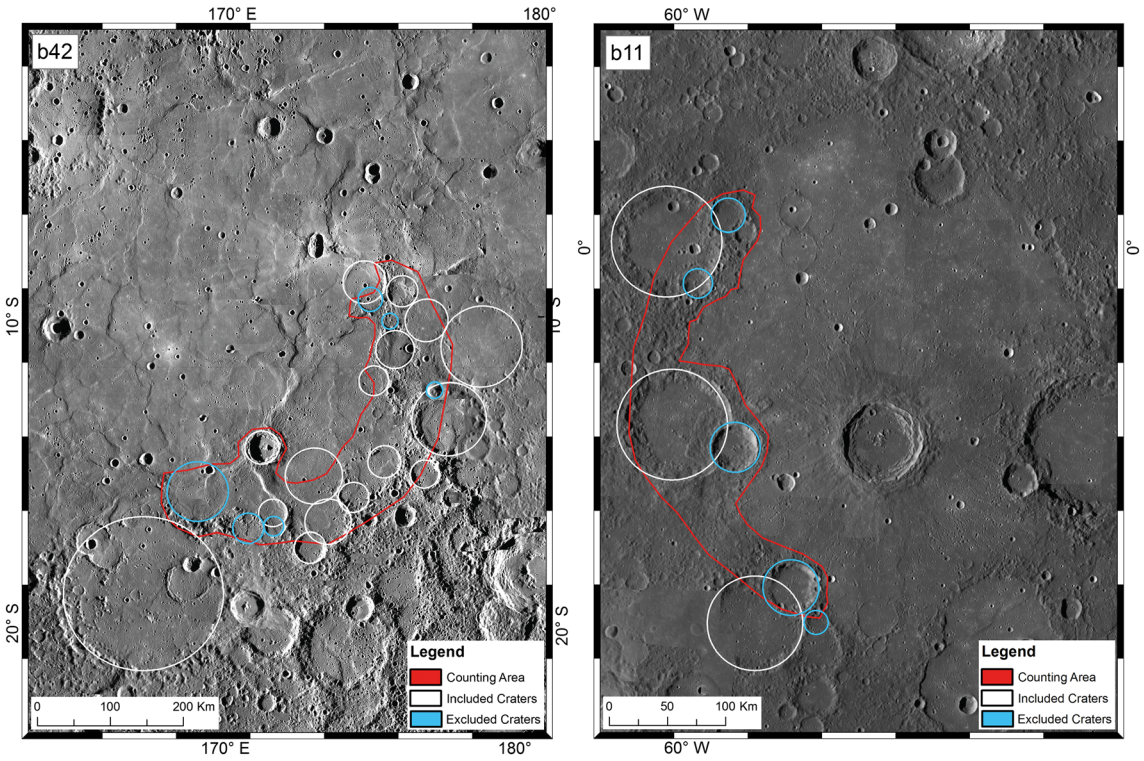

Figure 7. B42 has the largest difference between the BNSC and the BCC1 results (292%), while the discrepancy is the lowest (−44%) in b11. Craters excluded and included during computation are marked with blue and white, respectively.

correction typically leads to an increase of the obtained smaller crater densities when compared to the BCC technique (Figure 6).

As described in section 3, we derived the crater densities of Mercurian basins using two different CSFD techniques: BCC and BNSC. The differences in measured crater frequencies using BCC and BNSC become systematically larger for older surfaces, such as Pre-Tolstojan basins, than on younger surfaces, due to the increasing role that crater obliteration plays on older surfaces. Thus, the $N(25)$ values for Mercurian basins derived using the BNSC technique are different from the $N(25)$ values obtained using with the BCC1 technique. The shifting of the results is in good agreement with improvements made to lunar basin CSFDs in our previous study (Orgel et al., 2018). The application of BNSC increases the obtained $N(25)$ values by an average of 35% compared to BCC1 (Table 2). If we exclude the anomalously high crater density of b42, this value drops to 25%. This difference is slightly higher on Mercury than on the Moon, where we measured 24% increase (Orgel et al., 2018).

The b42 basin has the highest $N(25)$ crater frequency (745 ± 186). The difference (292%) between the BNSC and the BCC1 results for this basin are also the largest. The higher crater frequency can be explained by the exclusion of area that had been resurfaced by subsequent craters and their ejecta in a relatively small counting area (Figure 7 and supporting information). The discrepancy between the BNSC and BCC1 $N(25)$ values is lowest in b11 basin (−44%) (Figure 7 and supporting information). The negative factor shows a decreased crater frequency compared to BCC1. This effect could be interpreted as resulting from the distribution of few larger craters, which are separated from each other over relatively large area. Additionally, the centers of intersecting craters fall within one crater radius, thus, are excluded from the calculation due to obliteration.

4.3. Spatial Densities of Basins on Mercury and the Moon

The spatial densities of (1) certain and probable (altogether 80 basins) and (2) all basins including tentative basins (altogether 94 basins), respectively, allow a comparison between the basin populations on Mercury and the Moon. This can be done without rescaling the values of $N(300,500)_{\text{Moon}}$ to $N(X,Y)_{\text{Mercury}}$ due to

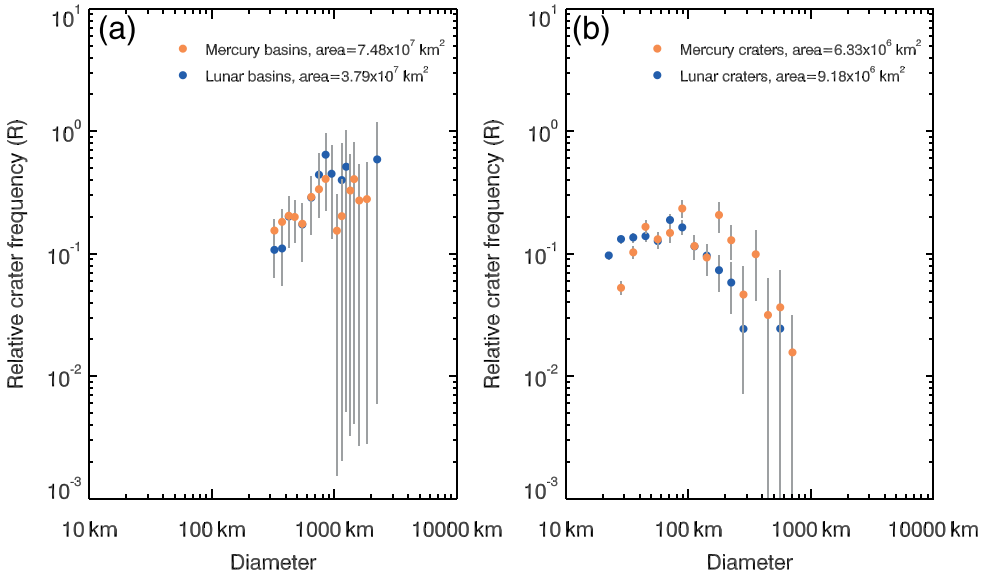

Figure 8. Relative crater frequency of (a) large basins ($D \geq 300$ km) and (b) craters superposing large basins on Mercury (Pre-Tolstojan, Tolstojan basins and Caloris), and compared to the Moon (Pre-Nectarian, Nectarian, and Imbrian basins) (Orgel et al., 2018).

the large uncertainties in scaling at basin scales. The spatial density of basins with $D \geq 300$ km per 10^6 km^2 on Mercury or the $N(300)_{\text{Mercury}}$ are 1.07 ± 0.12 (certain and probable) and 1.26 ± 0.13 (all basins), respectively. Similarly, the spatial density of basins with $D \geq 500$ km per 10^6 km^2 on Mercury or the $N(500)_{\text{Mercury}}$ are 0.44 ± 0.07 (certain and probable) and 0.54 ± 0.08 (all basins), respectively. To compare the basin density values with the updated data set from the Moon, we derived the spatial density of lunar basins (altogether 36 basins) using the data from Orgel et al. (2018) with additional basins from the Neumann et al. (2015) basin catalog. We found that the spatial density of basins with $D \geq 300$ km and $D \geq 500$ km per 10^6 km^2 are an $N(300)_{\text{Moon}}$ of 0.94 ± 0.16 and an $N(500)_{\text{Moon}}$ of 0.55 ± 0.12. In contrast to a previous study (Fassett, Head, Baker, et al., 2012), we find that basins have a slightly higher $N(300)$ density on Mercury than on the Moon (Figure 8a), but the difference is below the level of the 1-sigma uncertainties. The similar $N(500)$ basin density on Mercury and the Moon has substantial implications for the early history of both planetary bodies′ crust. This result could be the consequence of saturation on both surfaces (Fassett et al., 2011).

We also summed the crater densities of certain and probable Mercurian (Pre-Tolstojan, Tolstojan basins and Caloris basin, altogether 29 basins) and lunar basins (Pre-Nectarian, Nectarian and Imbrian basins, altogether 36 basins) (see also Orgel et al., 2018) using the BNSC technique, alone (Figure 8b). Compared to the Moon, the crater densities on Mercury are slightly higher or nearly equivalent at large crater diameters ($D > 100$ km). Below 100 km in diameter, the CSFD on Mercury falls below the lunar distribution, which is consistent with previous studies (Fassett et al., 2011; Fassett, Head, Baker, 2012).

4.4. Impactor Population

To investigate the nature of the impactor population(s) on Mercury, we compared the summed BNSC CSFDs of the Pre-Tolstojan-aged basins and Tolstojan-aged basins (including Tolstoj) (Figures 9c and 9d) to one another, and then to the summed CSFDs of Pre-Nectarian, Nectarian, and Imbrian basins on the Moon (Figures 9a and 9b) (Orgel et al., 2018). Figure 9a shows that Pre-Nectarian CSFD does not conform to the isochrons of the unchanging Neukum (1983) PF using the BCC method (Fassett, Head, Kadish, et al., 2012), concluding a change in impactor populations. The application of the BNSC method to the lunar basin population (Figure 9b) allowed the correction of the smaller crater size bins on ancient Pre-Nectarian surfaces (Orgel et al., 2018). By removing areas that were affected by nonsparse cratering, and thus the destruction of smaller diameter craters by subsequent craters and their ejecta, a clearer view of the Pre-Nectarian CSFD was possible. Indeed, Orgel et al. (2018) were able to conclude that the shape of the CSFD between

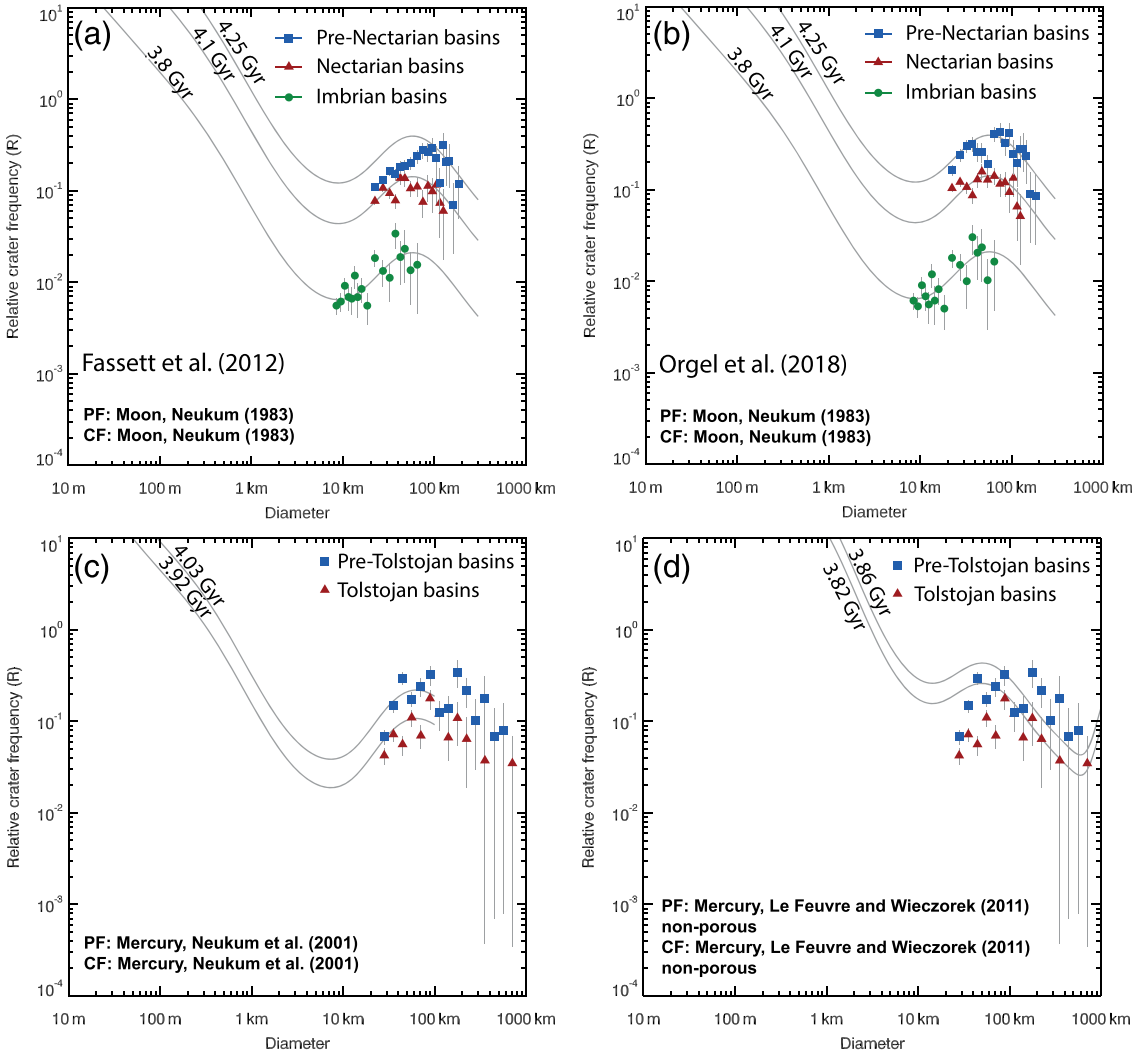

Figure 9. Summed CSFDs to study the impactor population(s) on the Moon (a, b) and Mercury (c, d) using an R-plot representation. (a, b) Summed CSFDs of the Pre-Nectarian-aged basins (excluding SPA, blue squares), Nectarian-aged basins (red triangles) and Imbrian-aged basins (green circles) on the Moon using the BNSC technique (30 basins). The gray lines represent the isochrons of the PF. (a) Fassett, Head, Kadish, et al. (2012) found a steep slope in the diameter range from 20 to 100 km in the shape of Pre-Nectarian CSFD using the BCC method (Fassett & Head, 2008) and concluded different impactor populations (modified from Orgel et al., 2018). (b) In contrast, Orgel et al. (2018) show that CSFDs conform to the Neukum (1983) PF showing an unchanging shape of the distribution, thus indicating an unchanging SFD of impactors (modified from Orgel et al., 2018). (c, d) Summed CSFDs of the Pre-Tolstojan-aged basins (blue squares) and Tolstojan-aged basins (red squares) on Mercury using the BNSC technique (29 basins). (c) The shape of CSFDs does not follow the Neukum et al. (2001) PF below 35km diameter in Pre-Tolstojan distribution. (d) The summed CSFDs do not conform to the Le Feuvre and Wieczorek (2011) nonporous PF below ~50km diameter, but they fit at larger crater sizes.

the Pre-Nectarian, Nectarian, and Imbrian periods did not change, which suggests that the SFD of the impacting population did not change as had previously been suggested (Fassett, Head, Kadish, et al., 2012; Head et al., 2010).

The shapes of the CSFDs for the Pre-Tolstojan and Tolstojan periods have similar shapes that generally follow the trend of the Neukum et al. (2001) PF (Figure 9c) but do not conform to the Le Feuvre and Wieczorek (2011) PF for nonporous material (Figure 9d). As expected, the Pre-Tolstojan data set plots above the Tolstojan due to their relative age differences. It is difficult to tell based on the spread of the data points around the example isochrons whether there is a significant difference between the shapes of the two curves. Potentially, the smaller crater bins in the Pre-Tolstojan exhibit a lower crater spatial density than later in the Tolstojan.

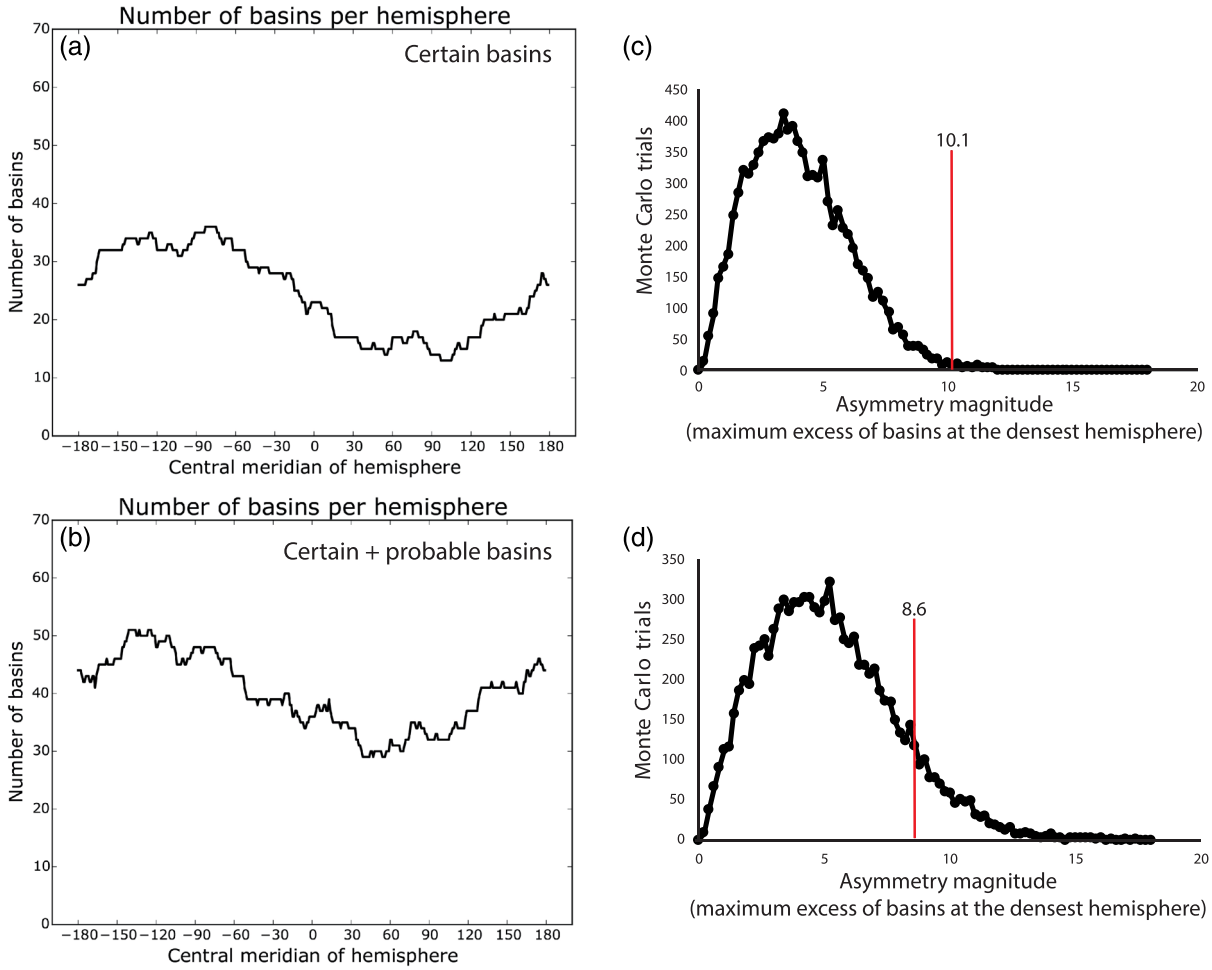

Figure 10. Basin asymmetry based on (a) *certain* and (b) *certain* and *probable* basins. Number of basins per hemisphere shown in each 1° increments. The axes show the frequency of basins (*y* axis) for a hemisphere with a given central meridian (*x* axis); note that the dividing line between these two hemispheres is thus $x + 90°$. (c) Monte Carlo simulation of the probability to form *certain,* and (d) *certain* and *probable* basins on the surface. The axes show the Monte Carlo trials (*y* axis) to recreate the observed basin distribution, and the asymmetry magnitude (*x* axis) represents the maximum excess of basins at the densest hemisphere. We found certain basins would have a lower basin asymmetry magnitude in 98% of cases with 10.1 asymmetry magnitude (red line), than the observed distribution (panel c). While, certain and probable basins would do so in 91% of trials with 8.6 basin asymmetry magnitude (red line) (panel d).

5. Discussion

5.1. Geographic Distribution of Basins

Fassett, Head, Baker, et al. (2012) suggested that the geographic distribution of the basins on the surface of Mercury is nonuniform. There are fewer basins observed on the eastern hemisphere than on the western hemisphere.

To analyze whether the basin distribution on Mercury is consistent with being drawn from a random population, we investigated the number of basins in hemispheres across the planet with a central meridian every 1° in longitude. Figures 10a and 10b show the number of basins is maximal for a hemisphere centered at roughly 120°W ± 30°, with a corresponding lower frequency in the opposite hemisphere. We ran a Monte Carlo simulation to test the probability of seeing a comparable magnitude for the observed basin asymmetry. We found certain basins would have a lower basin asymmetry magnitude in 98% of cases, while certain and probable basins would do so in 91% of trials (Figures 10c and 10d). Note that this is a statistical probability calculation, where basins are treated as points, and target properties and geologic processes are assumed to be homogenous. Nonetheless, it tentatively suggests that the asymmetry in basin distribution would not be expected if basins were emplaced on the surface in a random manner.

Table 4
AMA Intervals for Pre-Tolstojan and Tolstojan Basins

	Neukum et al. (2001) AMA intervals (Gyr)	Neukum et al. (2001) avg. AMA (Gyr)	Le Feuvre and Wieczorek (2011) AMA intervals (Gyr)	Le Feuvre and Wieczorek (2011) avg. AMA (Gyr)
Pre-Tolstojan basins	Max.$4.24^{+0.04}_{-0.06}$ (Borealis)	$4.05^{+0.06}_{-0.15}$	Max.$3.95^{+0.02}_{-0.03}$ (Borealis)	$3.84^{+0.03}_{-0.04}$
	Min.$3.94^{+0.06}_{-0.07}$ (b38)		Min.$3.75^{+0.03}_{-0.06}$ (b38)	
Tolstojan basins	Max.$4.10^{+0.05}_{-0.07}$ (b12)	$3.96^{+0.05}_{-0.06}$	Max.$3.94^{+0.05}_{-0.07}$ (b20)	$3.79^{+0.04}_{-0.07}$
	Min.$3.85^{+0.05}_{-0.06}$ (Beethoven)		Min.$3.65^{+0.04}_{-0.15}$ (Rembrandt)	

This distribution could be explained by three major hypotheses: (1) different thermal properties of the crust due to orbital resonances and/or interior geodynamical processes (Chapman et al., 2018; Miljkovíc et al., 2013; Siegler et al., 2013; Vasavada, 1999), (2) differential resurfacing by volcanism (Fassett, Head, Baker, et al., 2012; Denevi, Ernst, Meyer, et al., 2013), or (3) that the basins on Mercury are spatially random but happened to end up in this configuration.

In the present day, Mercury's 3:2 spin-orbit coupling leads to a ~150-K difference in crustal temperatures as a function of longitude between the so-called "hot pole" (at 0°E and 180°E) and "cold pole" (at 90°E and 270°E) longitudes. Moreover, there is a ~150- to 300-K difference with latitude, with the larger contrast in the hot pole longitudes, which substantially depend on the orbital eccentricity (Vasavada et al., 1999; Williams et al., 2011). The orbital eccentricity of Mercury varied between 0.0 and 0.4 over its history (Correia & Laskar, 2004), and thus, the magnitude of lithospheric temperature anomalies may have varied substantially over billions of years. A complication for the importance of this effect is that it remains an open question when Mercury reached the 3:2 resonances (e.g., Tosi et al., 2015: >1 Gyr after formation; Noyelles et al., 2014: <20 Myr) that set up the current lithospheric thermal structure. If this happened well into Mercury's history, it is plausible that no differences in the observed SFD as a function of lithospheric temperature would be expected, even with Mercury's present inhomogeneous distribution of temperature. Alternatively, Mercury might have once reached 1:1 spin-orbital resonance during its history with one hemisphere always facing the Sun and causing significant surface temperature difference on both sides (Correia & Laskar, 2009; Wieczorek et al., 2012). This thermal contrast could translate into differences in crater size, morphology, or morphometry, particularly for large impact events. The National Aeronautics and Space Administration's Gravity Recovery and Interior Laboratory(NASA's GRAIL) confirmed that the basins on the Moon are larger on the nearside than on the far side (Neumann et al., 2015). This asymmetry was explained by the increase of the heat-producing elements on the nearside; consequently, the nearside was initially hotter than the farside (Miljkovíc et al., 2013). Miljkovíc et al. (2013) used the iSALE-2D hydrocode to model the SFD of basins on both hemispheres and found that lateral variations in target temperature could have greatly affected the SFD of basins. Specifically, the warmer nearside results in a SFD that shifts to larger crater diameters and hence larger diameter of basins on the warm hemisphere.

The second major hypothesis is that the formation of smooth plains is spatially nonuniform on the surface and coincides with basins; however, one third of the smooth plains is located in the northern polar region unrelated to any large basin forming impacts (Denevi, Ernst, Meyer, et al., 2013; Ostrach et al., 2015; Qingyun et al., 2018). The thickness of smooth plains varies between 0.5 and 4 km (Denevi et al., 2009; Denevi, Ernst, et al., 2018; Denevi, Ernst, Meyer, et al., 2013; Ernst et al., 2015; Head et al., 2009, 2011; Ostrach et al., 2015; Prockter et al., 2010; Trask & Guest, 1975; Whitten & Head, 2015). We observe basins ($D \geq 300$ km) completely infilled by smooth plains and outlined by wrinkle ridges or lobate scarps. Of course, the effectiveness of this large-scale resurfacing process is dependent on basin size and the thickness of volcanic plains. Thus, the complete erasure of basins cannot be excluded by a planet-wide differential resurfacing.

5.2. Basin Formation and Subsequent Geologic Activity

In this study, we derived the AMAs of individual basins using the CSFDs we measured using the BNSC technique. The AMAs are dependent on the chronology model, which in fact is extrapolated from the lunar one and thus, includes uncertainties (Le Feuvre & Wieczorek, 2011; Neukum et al., 2001). We compared the

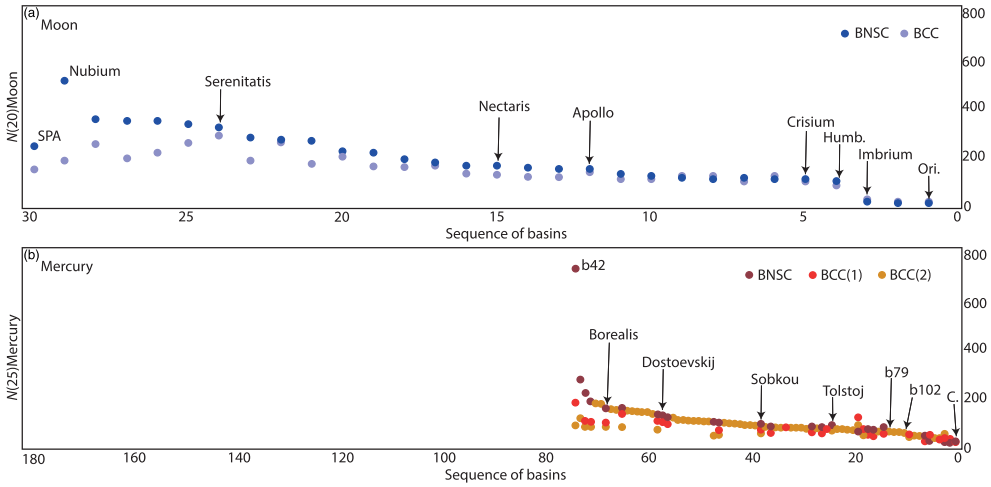

Figure 11. Sequence of basin formation on the Moon (a) and Mercury (b). Crater densities derived with (i) BNSC and (ii) BCC techniques with two different mapping techniques on Mercury: BCC1 measuring craters excluding all areas resurfaced by the smooth plains and, BCC2 mapping all craters inside the basin cavity. Crater densities derived with BNSC commonly show a higher density than with BCC technique on both planetary surfaces. Note the number of lunar and Mercurian basins is 30 (Orgel et al., 2018) and 74, respectively. However, we assume that the Moon has 36 lunar basins (including six additional basins from Neumann et al., 2015) larger than 300 km after the lunar magma ocean solidification, we should observe ~5 times more basins (2.5 times higher crater production rate above 300 km and a factor of 2 greater surface area) to form on Mercury than on the Moon. Consequently, we expect to observe ~180 basins on Mercury. Lunar basins are spaced at a 5 times interval to compensate for the higher impact rate and larger surface area on Mercury than the Moon; thus, roughly five basins should form for every lunar basin. Key basins are highlighted in the upper right corner of the symbols and with arrows. Abbreviations: C. = Caloris basin, SPA = South Pole Aitken basin, Humb. = Humboldtianum basin, Ori. = Orientale basin, lunar data are from Orgel et al. (2018).

results derived with the Neukum et al. (2001) and Le Feuvre and Wieczorek (2011) nonporous chronology models and found a ~200Myr difference between the AMAs (Figure 6 and Table 4). We found that the AMAs for Pre-Tolstojan basins (Neukum et al., 2001) range from $4.24 \pm 0.04/0.06$ Gyr (Borealis basin) to $3.94 \pm 0.06/0.07$ Gyr (b38) with an average AMA of $4.05 \pm 0.06/0.15$ Gyr, whereas the AMA of Pre-Tolstojan basins using the Le Feuvre and Wieczorek (2011) CF vary between $3.95 \pm 0.02/0.03$ Gyr (Borealis basin) and $3.75 \pm 0.03/0.06$ Gyr (b38) with an average AMA of $3.84 \pm 0.03/0.04$ Gyr. The AMAs of Tolstojan basins using the Neukum et al. (2001) CF give results from $4.10 \pm 0.05/0.07$ Gyr (b12) to $3.85 \pm 0.05/0.06$ Gyr (Beethoven basin) with an average AMA of $3.96 \pm 0.05/0.06$ Gyr. Using the Le Feuvre and Wieczorek (2011) CF, the AMAs vary from $3.94 \pm 0.05/0.07$ Gyr (b20) to $3.65 \pm 0.04/0.15$ Gyr (Rembrandt basin) with an average of $3.79 \pm 0.04/0.07$ Gyr. Although we report AMAs to three significant digits, the systematic errors in the CF could be substantial (>200 Ma), and errors resulting from resurfacing are also nonnegligible (hundreds of million years). Thus, these values should be treated with appropriate caution.

The sequence of basins on Mercury was ranked based on $N(25)$ crater frequencies using the BNSC, BCC1, or BCC2 CSFD techniques. We found that $N(25)$ and relative stratigraphy are in good agreement, with only seven basins showing discrepancies (Table 2, marked with italics). Figure 11 shows the sequence of basin formation on Mercury (74 basins) and the Moon (30 basins) including results of all CSFD techniques. In Table 2, we include six more basins, but because of the absence of reliable crater statistics, we do not indicate these basins on Figure 11. Note that Mercurian basins with higher crater frequencies than Borealis are very few in number compared with the Pre-Nectarian lunar basins. The youngest large Mercurian basins (Rembrandt: 35 ± 7, BNSC, 36 ± 6, BCC1; Caloris: 35 ± 6, BNSC; 28 ± 7, BCC1) have a crater density when rescaled comparable to Imbrium and significantly higher than Schrödinger or Orientale. Rembrandt basin has been suggested to be similar in age or slightly older than Caloris (Fassett, Head, Baker, et al., 2012; Watters et al., 2009; Whitten & Head, 2015). According to this study, AMA and $N(25)$ of it is slightly higher than the Caloris forming event, although the error bars overlap in $N(25)$. We consider Rembrandt basin as probably having formed in the Tolstojan period, which is in agreement with previous studies (Ferrari et al., 2015; Gemperline et al., 2017; Hynek et al., 2016).

Based on the 2.5 times higher crater production rate above 300 km (Le Feuvre & Wieczorek, 2011) and a factor of 2 greater surface area, we expect a factor of ~5 more basins to form on Mercury than on the Moon

(Figure 11). Consequently, we should observe ~180 basins on Mercury, if we calculate with 36 lunar basins larger than 300 km using Orgel et al. (2018) data and 6 additional basins from Neumann et al. (2015). Note that the observed 36 lunar basins show only the basin record after the lunar magma ocean solidification, when the formation of impact basins was feasible on the solid surface. This study classified 94 basins, including 80 certain and probable as well as 14 tentative basins. Thus, we observe roughly half of the basin record, where older basins than Borealis are completely erased from the basin record, and this finding is in good agreement with Marchi et al. (2013). Their findings suggest global resurfacing processes related to heavy bombardment and persistent volcanic activity about 4.0–4.1 Gyr ago.

The questions are what happened to Mercury's surface prior 4.1 Gyr and where are the missing basins? Alternatively, other processes besides LHB and extensive volcanism could explain the absence of basins. These include (1) viscoelastic relaxation of impact basins (Conrad et al., 2018; Kamata et al., 2015) due to the aftermath of a prolonged global magma ocean (Brown & Elkins-Tanton, 2009; Vander Kaaden & McCubbin, 2015) by tidal heating (Meyer et al., 2010) or (2) enhanced impact melt production due to the higher impactor velocities (Barr & Citron, 2011; Cintala & Grieve, 1998; Gault, 1975; Manske et al., 2019; Ostrach et al., 2012; Pierazzo et al., 1997; Whitten & Head, 2015).

The first hypothesis is that the initial thermal conditions from planetary accretion and metal-silicate differentiation likely produced a global magma ocean on terrestrial planets and the Moon (Brown & Elkins-Tanton, 2009; Shearer et al., 2006). The cooling of the magma ocean led to fractional crystallization, where positively buoyant minerals formed a “primary” or “flotation” crust. Based on laboratory experiments, this mineral for Mercury is likely graphite, which originated from a low-FeO melt (Vander Kaaden & McCubbin, 2015). The remnants of that layer might be exposed now as low-reflectance material by larger impacts, which is significantly contributing to the low albedo of Mercury's surface (Denevi et al., 2009; Robinson et al., 2008). Furthermore, those basins that formed around or shortly after the solidification of the magma ocean exhibit viscoelastic relaxation and still might show observable structures. However, on the Moon most of the proposed old Pre-Nectarian basins on the Moon do not exhibit clear topographic or gravity signatures (Kamata et al., 2015). Kamata et al. (2015) investigated the viscoelastic deformation of impact basins on the Moon using crustal thickness models to infer their thermal state at the time of basin formation. They find that a Moho temperature >1300–1400 K is required for substantial viscous relaxation of the topography, and such a high temperature can be maintained only for a short time (<50 Myr), or after a possible mantle overturn ≥150 Myr after magma ocean solidification. However, the magma ocean solidification may have been prolonged by tidal heating for 200–300 Myr on the early Moon (Meyer et al., 2010). Conrad et al. (2018) drew the same conclusions from GRAIL, where they assessed the age and relaxation state of lunar impact basins and find a change in relaxation state likely caused by the cooling of the lunar crust between 4.21 and 4.45 Gyr. The solidification time of the magma ocean on Mercury is unknown, but similar processes could have affected Mercury's early crustal evolution (Padovan et al., 2015).

Second, considering higher impact rates, impact melt production was dominant in the early history of Mercury (Cintala & Grieve, 1998; Gault, 1975; Ostrach et al., 2012; Whitten & Head, 2015) and even more intensive than on the Moon. Manske et al. (2019) used hydrocode simulations to determine the amount of melt generated by an impact and found that the interior temperature and lithospheric pressure of the target planet significantly affects the final melt distribution and the crater morphology for impactors larger than 10 km in diameter on Mars. Additionally, large-scale collisions on a younger and hotter planet may result in the formation of an impact melt pool to fill up the entire crater resulting in the formation of an igneous province rather than a typical basin structure (Manske et al., 2019). This scenario could be relevant for Mercury, where the oldest basins are not observable on the surface. One plausible explanation is that they drowned in their own melt.

5.3. Saturation Equilibrium

Saturation equilibrium is reached when the formation of new craters and their ejecta obliterate (on average) an equal number of preexisting craters (Gault, 1970; Shoemaker, 1965; Woronow, 1977).

To investigate the possibility of saturation equilibrium on Mercury in crater diameters ≥25 km, we compared the fraction of the original and the BNSC modified count area sizes for each basin to its $N(25)$ crater frequencies (Figure 12a). We expect that basins that show the highest level of nonsparseness to be close to or

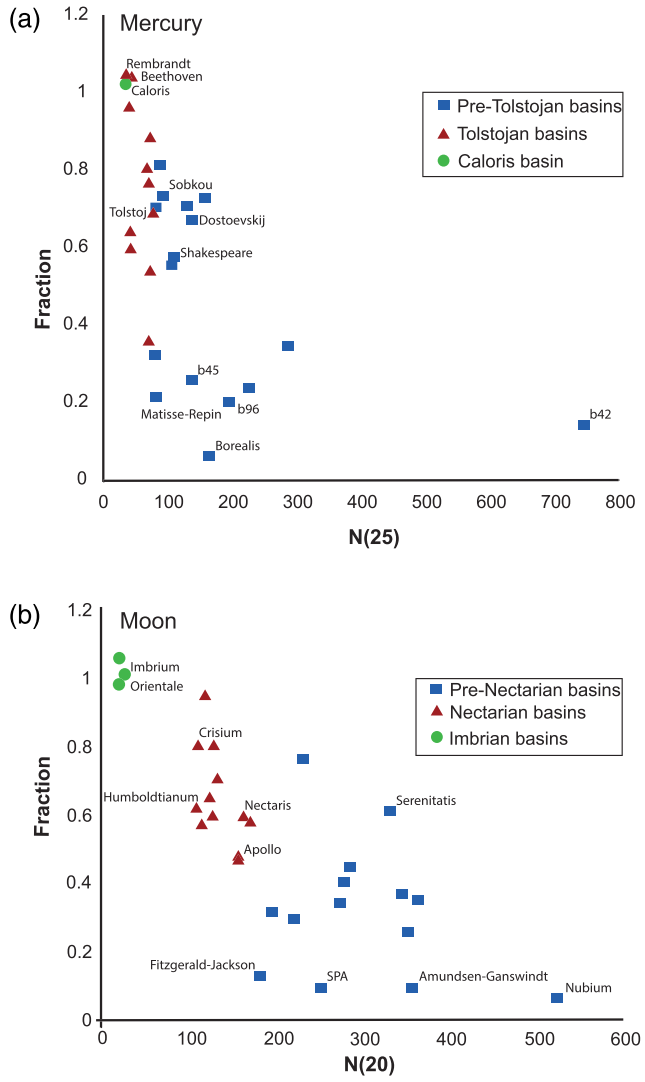

Figure 12. Comparison of $N(20,25)$ versus fraction of original and BNSC-modified count area on Mercury (a) and the Moon (b). The BNSC-modified count area is the area size related to the smallest crater after computation. The diagrams present the decrease of the remaining area after the BNSC correction and the increase of the $N(20,25)$ value toward older surfaces. Fraction is calculated by 1.0 divided by the original count area size/BNSC-modified area size. Where the count area size/buffer area size is smaller than 1.0, the determined fraction could be larger than 1.0. (a) Borealis, Matisse-Repin, b96, and b42 might be in saturation equilibrium on Mercury, where their original count area is less than 20% (fraction = 0.2). The $N(25)$ value derived by the BNSC technique of the corresponding basins is listed in Table 2. (b) Fitzgerald-Jackson, South Pole-Aitken (SPA), Amundsen-Ganswindt, and Nubium might be in saturation equilibrium on the Moon, where their original count area is less than 20%, lunar data are from Orgel et al. (2018).

at saturation equilibrium. We observe a linear decrease in the effective counting area with increasing $N(25)$ value toward older surfaces, because the level of nonsparseness increases with basin age. This finding is in good agreement with the trends in saturation equilibrium of the lunar basins at diameters ≥20 km (Orgel et al., 2018). However, this linear decrease is steeper than on the Moon (Figure 12b), which might provide additional evidence for an absence of basins older than Borealis on Mercury.

For example, Caloris, Beethoven, and Rembrandt basins' BNSC $N(25)$ values are calculated using nearly 100% of the original count area. Accordingly, the nonsparseness effect is negligible; we observed the same characteristic in the youngest basins on the Moon (Orgel et al., 2018). Consequently, these basins could belong to the same geologic time period. $N(25)$ values for Tolstojan basins are based on 40–90% of the initial count area, while most $N(25)$s for Pre-Tolstojan basins were derived from 10–70% of the original areas.

At the largest crater diameters, four Pre-Tolstojan basins (Borealis, Matisse-Repin, b96, and b42) have less than 20% of their original count area remaining after the implementation of the BNSC (Figure 12a and Table 2). This suggests that these basins have almost reached saturation equilibrium at crater diameters of ≤25 km and that only 10–20% of their remaining count areas represent unmodified surfaces. Note that the crater population observed upon basins at, or close to, saturation cannot provide reliable AMAs due to the reduced number of craters that can be used for the fit. Thus, even though we provide AMAs in Table 2, those with the highest crater densities should be interpreted cautiously. The relatively small number of basins (Borealis, Matisse-Repin, b96, and b42) are saturated with craters that have diameters of ≤25 km, a conclusion consistent with previous results on the Moon (Fassett, Head, Kadish, et al., 2012; Head et al., 2010; Orgel et al., 2018; Povilaitis et al., 2017; Xiao & Werner, 2015). The BNSC method is, thus, useful for understanding the equilibrium conditions on Mercury and the Moon.

5.4. Impactor Population(s) and the LHB

Based on the observed crater populations on the Moon, Mars, and Mercury, Strom et al. (2005, 2011, 2015) and Head et al. (2010) proposed two different populations of impactors. Fassett, Head, Kadish, et al. (2012) found a steep slope in the diameter range from 20 to 100 km in the summed CSFDs of the Pre-Nectarian basins on the Moon and concluded that the impactor population changed in nature earlier than the mid-Nectarian period (Figure 9a). However, Orgel et al. (2018) found that the steep slope is removed when the new BNSC technique is applied to the measurement of CSFDs on heavily cratered lunar basin (Figure 9b). As a result, the CSFDs more closely follow the Neukum (1983) PF for all periods. This means that the shape of the impactor SFD across the Pre-Nectarian, Nectarian, and Imbrian periods did not change (Orgel et al., 2018). This implies that there was either one population of impactors or different populations with the same SFD.

One of the goals of our current work was to evaluate the nature of the impactor population(s) on Mercury using the same approach as for the Moon. We find that applying the BNSC to the CSFDs for the Mercurian basins gives $N(25)$ densities that are on average 25% (excluding b42) higher than when using BCC approaches alone. The observed increase in crater densities using BNSC in the CSFDs come from the improved accounting of the small crater populations on these highly cratered surfaces by excluding areas

where geometric crater obliteration occurred. This effect results in an increase in the measured crater spatial densities in these diameter bins, similar to what was seen for the BNSC on lunar data.

Again, if the Neukum (1983) and Neukum et al. (2001) theory that the impactor population in the inner solar system did not change over time, we would expect that the CSFDs for Mercurian basins in different time periods maintain a single shape following the PF. With our new data analyses, we find that the shapes of the Pre-Tolstojan and Tolstojan basins are similar, although it is not possible to say conclusively whether the SFD of the Pre-Tolstojan basins drops off more sharply at <50km diameters due to the scatter of the data set around the PF, which is more consistent with the Neukum et al. (2001) PF than the Le Feuvre and Wieczorek (2011) nonporous model. Above 50-km diameters, the SFDs of both time periods show similar shapes and slopes. In summary, while inconclusive for craters <50km diameter, our results support a single impactor population or different populations with the same impactor SFD for Mercury. This study does not preclude changes to the CSFD in more recent epochs, that is, in the Calorian and younger periods (Banks et al., 2017; Strom et al., 2011).

6. Conclusions

Altogether, we cataloged 94 basins, 1.7 times *certain* and *probable* basins as many as in earlier work (Fassett, Head, Baker, et al., 2012). We performed CSFD analysis of 74 basins using the BCC and the BNSC techniques. Applying the BCC technique only allowed us to determine minimum values for CSFDs, so the relative ages of these basins are uncertain. The BNSC proved to be a useful technique to correct the effect of geometric crater obliteration due to heavy cratering on Mercury, which was successfully applied in previous study of the Moon (Orgel et al., 2018). Based on the CSFDs, we established a relative basin sequence, which proved to be generally in good agreement with the observed relative basin stratigraphy. We estimated that roughly half of the expected basin record is missing, where basins older than Borealis have been obscured by different processes (e.g., higher impact melt production, volcanism, subsequent impacts, and viscoelastic relaxation of basins)—a finding is in agreement with Marchi et al. (2013). We investigated the summed CSFDs of Pre-Tolstojan and Tolstojan basins to shed light on the impactor populations. In contrast to previous studies (Fassett, Head, Baker, et al., 2012; Fassett, Head, Kadish, et al., 2012; Head et al., 2010; Marchi et al., 2013; Strom et al., 2015), which demonstrate a change in the shape of the CSFDs prior 3.9 Gyr, our results are consistent with Orgel et al. (2018) that one impactor population can explain the bombardment history of the surface of Mercury.

Acknowledgments

We would like to thank Lillian R. Ostrach and an anonymous reviewer for their helpful comments that improved this manuscript. C. O., C. R., and H. H. were funded by the Deutsche Forschungsgemeinschaft (DFG, German Research Foundation) - Project-ID 263649064 - TRR 170. This is TRR 170 Publication No. 98. C. F. was supported by a NASA Discovery Data Analysis Program grant, Analysis of Large-scale Resurfacing Processes on Mercury. G. M. was supported by the German Aerospace Center (Deutsches Zentrum für Luft- und Raumfahrt) Project 50QM1702 and C. H. vdB Project 50OW1504. All the raw data for this work are available on the NASA Planetary Data System (PDS). The derived data products are at https://doi.org/10.17632/vf2sfbdvzr.1. The dataset can be cited as Orgel, Csilla; Fassett, Caleb; Michael, Gregory; Riedel, Christian; van der Bogert, Carolyn H.; Hiesinger, Harald (2020), "Re-examination of the population, stratigraphy, and sequence of mercurian basins: Implications for Mercury's early impact history and comparison with the Moon", Mendeley Data, V1, doi: 10.17632/vf2sfbdvzr.1.

References

Ackiss, S. E., Buczkowski, D. L., Ernst, C. M., McBeck, J. A., & Seelos, K. D. (2015). Knob heights within circum-Caloris geologic units on Mercury: Interpretations of the geologic history of the region. *Earth and Planetary Science Letters*, *430*, 542–550.

Arvidson, R., Boyce, J., Chapman, C., Cintala, M., Fulchignoni, M., Moore, H., et al. (1978). Crater analysis techniques working group—Standard techniques for presentation and analysis of crater size-frequency data. NASA Technical Memorandum 79730, Washington, D.C.

Baker, D. M. H., & Head, J. W. (2013). New morphometric measurements of craters and basins on Mercury and the Moon from MESSENGER and LRO altimetry and image data: An observational framework for evaluating models of peak-ring basin formation. *Planetary and Space Science*, *86*, 91–116.

Baker, D. M. H., Head, J. W., Schon, S. C., Ernst, C. M., Prockter, L. M., Murchie, S. L., et al. (2011). The transition from complex crater to peak-ring basin on Mercury: New observations from MESSENGER flyby data and constraints on basin-formation models. *Planetary and Space Science*, *59*, 1932–1948. https://doi.org/10.1016/j.pss.2011.05.010

Baldwin, R. B. (1971). On the history of lunar impact cratering: The absolute time scale and the origin of Planetesimals. *Icarus*, *14*, 36–52.

Baldwin, R. B. (2006). Was there ever a Terminal Lunar Cataclysm? With lunar viscosity arguments. *Icarus*, *184*(2), 308–318.

Banks, M. E., Xiao, Z., Braden, S. E., Barlow, N. G., Chapman, C. R., Fassett, C. I., & Marchi, S. S. (2017). Revised constraints on absolute age limits for Mercury's Kuiperian and Mansurian stratigraphic systems. *Journal of Geophysical Research: Planets*, *122*, 1010–1020. https://doi.org/10.1002/2016JE005254

Barr, A. C., & Citron, R. I. (2011). Scaling of melt production in hypervelocity impacts from high-resolution numerical simulations. *Icarus*, *211*(1), 913–916.

Becker, K. J., Robinson, M. S., Becker, T., Weller, L. A., Edmundson, K. L., Neumann, G. A., et al. (2016). First global digital elevation model of Mercury. 47th Lunar and Planetary Science Conference, 47, #2959, The Woodlands, TX.

Braden, S. E., & Robinson, M. S. (2013). Relative rates of optical maturation of regolith on Mercury and the Moon. *Journal of Geophysical Research: Planets*, *118*, 1903–1914. https://doi.org/10.1002/jgre.20143

Brown, S. M., & Elkins-Tanton, L. T. (2009). Compositions of Mercury's earliest crust from magma ocean models. *Earth and Planetary Science Letters*, *286*, 446–455.

Byrne, P. K., Klimczak, C., & Sengör, A. M. C. (2018). The tectonic character of mercury. In S. C. Solomon, L. R. Nittler, & B. J. Anderson (Eds.), *Mercury: The view after MESSENGER* (pp. 249–286). University of Cambridge, Cambridge, UK: Cambridge University Press.

Byrne, P. K., Klimczak, C., Sengör, A. M. C., Solomon, S. C., Watters, T. R., & Hauck, S. A. II. (2014). Mercury's global contraction much greater than earlier estimates. *Nature Geoscience*, *7*, 301–307.

Byrne, P. K., Ostrach, L. R., Fassett, C. I., Chapman, C. R., Denevi, B. W., Evans, A. J., et al. (2016). Widespread effusive volcanism on Mercury likely ended by about 3.5 Ga. *Geophysical Research Letters*, *43*, 7408–7416. https://doi.org/10.1002/2016GL069412

Cavanaugh, J. F., Smith, J. C., Sun, X., Bartels, A. E., Ramos-Izquierdo, L., Krebs, D. J., et al. (2007). The Mercury Laser Altimeter Instrument for the MESSENGER Mission. Spacecraft. *Space Science Reviews*, *131*(1-4), 451–479. https://doi.org/10.1007/s11214-007-9273-4

Chabot, N. L., Denevi, B. W., Murchie, S. L., Hash, C. D., Ernst, C. M., Blewett, D. T., et al. (2016). Mapping Mercury: Global imaging strategy and products from the MESSENGER mission. 47th Lunar and Planetary Science Conference, 47, #1256, The Woodlands, TX.

Chapman, C. R., Baker, D. M. H., Barnouin, O. S., Fassett, C. I., Marchi, S., Merline, W. J., et al. (2018). Impact cratering of Mercury. In S. C. Solomon, L. R. Nittler, & B. J. Anderson (Eds.), *Mercury: The view after MESSENGER* (pp. 217–248). University of Cambridge, Cambridge, UK: Cambridge University Press.

Chapman, C. R., & McKinnon, W. B. (1986). Cratering of planetary satellites. In J. A. Burns, & M. S. Matthews (Eds.), *Satellites* (pp. 492–580). Tucson: University of Arizona Press.

Cintala, M. J., & Grieve, R. A. F. (1998). Scaling impact melting and crater dimensions: Implications for the lunar cratering record. *Meteoritics & Planetary Science*, *33*, 889–912.

Conrad, J. W., Nimmo, F., Fassett, C. I., & Kamata, S. (2018). Lunar impact history constrained by GRAIL-derived basin relaxation measurements. *Icarus*, *314*, 50–63.

Correia, A. C. M., & Laskar, J. (2004). Mercury's capture into 3/2 spin-orbit resonance as a result of its chaotic dynamics. *Nature*, *429*(6994), 848–850. https://doi.org/10.1038/nature02609

Correia, A. C. M., & Laskar, J. (2009). Mercury's capture into the 3/2 spin–orbit resonance including the effect of core–mantle friction. *Icarus*, *201*, 1–11.

Denevi, B. W., Chabot, N. L., Murchie, S. L., Becker, K. J., Blewett, D. T., Domingue, D. L., et al. (2018). Calibration, projection, and final image products of MESSENGER's Mercury Dual Imaging System. *Space Science Reviews*, *214*(1), 1, 2–52. https://doi.org/10.1007/s11214-017-0440-y

Denevi, B. W., Ernst, C. M., Meyer, H. M., Robinson, M. S., Murchie, S. L., Whitten, J. L., et al. (2013). The distribution and origin of smooth plains on Mercury. *Journal of Geophysical Research: Planets*, *118*, 891–907. https://doi.org/10.1002/jgre.20075

Denevi, B. W., Ernst, C. M., Prockter, L. M., & Robinson, M. S. (2018). The geologic history of Mercury. In *Solomon, S. C., Nittler, L. R., Anderson, B. J. (Eds), Mercury: The view after MESSENGER* (pp. 144–175). University of Cambridge, Cambridge, UK: Cambridge University Press.

Denevi, B. W., Ernst, C. M., Whitten, J. L., Head, J. W., Murchie, S. L., Watters, T. R., et al. (2013). The volcanic origin of a region of intercrater plains on Mercury. In *44th Lunar and Planetary Science Conference, 44, #1218*. The Woodlands: TX.

Denevi, B. W., Robinson, M. S., Solomon, S. C., Murchie, S. L., Blewett, D. T., Domingue, D. L., et al. (2009). The evolution of Mercury's crust: A global perspective from MESSENGER. *Science*, *324*(5927), 613–618. https://doi.org/10.1126/science.1172226

Denevi, B. W., Seelos, F. P., Ernst, C. M., Keller, M. R., Chabot, N. L., Murchie, S. C., et al. (2016). Final calibration and multispectral map products from the Mercury Dual Imaging System Wide-Angle Camera on MESSENGER. 47th Lunar and Planetary Science Conference, 47, #1264, The Woodlands, TX.

Elkins-Tanton, L. T., & Hager, H. B. (2005). Giant meteoroid impacts can cause volcanism. *Earth and Planetary Science Letters*, *239*, 219–232.

Ernst, C. M., Denevi, B. W., Barnouin, O. S., Klimczak, C., Chabot, N. L., Head, J. W., et al. (2015). Stratigraphy of the Caloris basin, mercury: Implications for volcanic history and basin impact melt. *Icarus*, *250*, 413–429.

Fassett, C. I., & Head, J. W. (2008). The timing of Martian valley network activity: Constraints from buffered crater counting. *Icarus*, *195*, 61–89. https://doi.org/10.1016/j.icarus.2007.12.009

Fassett, C. I., Head, J. W., Baker, D. M. H., Zuber, M. T., Smith, D. E., Neumann, G. A., et al. (2012). Large impact basins on Mercury: Global distribution, characteristics, and modification history from MESSENGER orbital data. *Journal of Geophysical Research*, *117*, E00L08. https://doi.org/10.1029/2012JE004154

Fassett, C. I., Head, J. W., Blewett, D. T., Chapman, C. R., Dickson, J. L., Murchie, S. L., et al. (2009). Caloris impact basin: Exterior geomorphology, stratigraphy, morphometry, radial sculpture, and smooth plains deposits, Earth planet. *Science Letters*, *285*, 297–308. https://doi.org/10.1016/j.epsl.2009.05.022

Fassett, C. I., Head, J. W., Kadish, S. J., Mazarico, E., Neumann, G. A., Smith, D. E., & Zuber, M. T. (2012). Lunar impact basins: Stratigraphy, sequence and ages from superposed impact crater populations measured from Lunar Orbiter Laser Altimeter (LOLA) data. *Journal of Geophysical Research*, *117*, E00H06. https://doi.org/10.1029/2011JE003951

Fassett, C. I., Kadish, S. J., Head, J. W., Solomon, S. C., & Strom, R. G. (2011). The global population of large craters on Mercury and comparison with the Moon. *Geophysical Research Letters*, *38*, L10202. https://doi.org/10.1029/2011GL047294

Fegan, E. R., Rothery, D. A., Marchi, S., Massironi, M., Conway, S. I., & Anand, M. (2017). Late movement of basin-edge lobate scarps on Mercury. *Icarus*, *288*, 226–234.

Ferrari, S., Massironi, M., Marchi, S., Byrne, P. K., Klimczak, C., Martellato, E., & Cremonese, G. (2015). Age relationships of the Rembrandt basin and Enterprise Rupes Mercury. *Geological Society, London, Special Publications*, *401*(1), 159–172. https://doi.org/10.1144/SP401.20

Gault, D. E., Guest, J. E., Murray, J. B., Dzurisin, D., & Malin, M. C. (1975). Some comparisons of impact craters on Mercury and the Moon. *Journal of Geophysical Research*, *80*, 2444–2460.

Gault, D. E. (1970). Saturation and equilibrium conditions for impact cratering on the lunar surface: Criteria and implications. *Radio Science*, *5*(2), 273–291.

Gemperline, J., Hynek, B. M., Robbins, S. J., Osterloo, M. K., Mueller, K., & Thomas, R. (2017). Age estimates of geologic units around the Rembrandt basin, Mercury. 48th Lunar and Planetary Science Conference, Abstract #2864, The Woodlands, TX.

Hartmann, W. (1995). Planetary cratering I: Lunar highlands and tests of hypotheses on crater populations. *Meteoritics*, *30*, 451–467.

Hawkins, S. E., Boldt, J. D., Darlington, E. H., Espiritu, R., Gold, R. E., Gotwols, B., et al. (2007). The Mercury Dual Imaging System on the MESSENGER spacecraft. *Space Science Reviews*, *1-4*(131), 247–338.

Head, J. W., Chapman, C. R., Strom, R. G., Fassett, C. I., Denevi, B. W., Blewett, D. T., et al. (2011). Flood volcanism in the northern high latitudes of Mercury revealed by MESSENGER. *Science*, *333*(6051), 1853–1856. https://doi.org/10.1126/science.1211997

Head, J. W., Fassett, C. I., Kadish, S. J., Smith, D. E., Zuber, M. T., Neumann, G. A., & Mazarico, E. (2010). Global distribution of large lunar craters: Implications for resurfacing and impactor populations. *Science*, *329*(5998), 1504–1507. https://doi.org/10.1126/science.1195050

Head, J. W., Murchie, S. L., Prockter, L. M., Solomon, S. C., Chapman, C. R., Strom, R. G., et al. (2009). Volcanism on Mercury: Evidence from the first MESSENGER flyby for extrusive and explosive activity and the volcanic origin of plains. *Earth and Planetary Science Letters*, *285*, 227–242.

Howard, A. D. (2007). Simulating the development of Martian highland landscapes through the interaction of impact cratering, fluvial erosion, and variable hydrologic forcing. Geomorphology, 91. *Issues*, *3-4*, 332–363.

Hynek, B. M., Robbins, S. J., Mueller, K., Gemperline, J., Osterloo, M. K., & Thomas, R. (2016). Unlocking Mercury's geological history with detailed mapping of Rembrandt basin: Year 2. Annual Planetary Geologic Mappers Meeting, #7023, Flagstaff, AZ.

Ivanov, B. (2008). Size-frequency distribution of asteroids and impact craters: Estimates of impact rate. In V. V. Adushkin, & I. V. Nemchinov (Eds.), *Catastrophic events caused by cosmic objects* (pp. 91–116). Dordrecht, The Netherlands: Springer. https://doi.org/10.1007/978-1-4020-6452-4_4

Kamata, S., Sugita, S., Abe, Y., Ishihara, Y., Harada, Y., Morota, T., et al. (2015). The relative timing of Lunar Magma Ocean solidification and the Late Heavy Bombardment inferred from highly degraded impact basin structures. *Icarus*, *250*, 492–503.

Kneissl, T., Michael, G. G., Platz, T., & Walter, S. H. G. (2015). Age determination of linear surface features using Buffered Crater Counting approach—Case studies of the Sirenum and Fortuna Fossae graben systems on Mars. *Icarus*, *250*, 384–394.

Kneissl, T., Michael, G. G., & Schmedemann, N. (2016). Treatment of non-sparse cratering in planetary surface dating. *Icarus*, *277*, 187–195. https://doi.org/10.1016/j.icarus.2016.05.015

Kneissl, T., van Gasselt, S., & Neukum, G. (2011). Map-projection-independent crater size-frequency determination in GIS environments—New software tool for ArcGIS. *Planetary and Space Science*, *59*, 1243–1254. https://doi.org/10.1016/j.pss.2010.03.015

Kreslavsky, M. A., Head, J. W., Neumann, G. A., Zuber, M. T., & Smith, D. E. (2014). Kilometer-scale topographic roughness of Mercury: Correlation with geologic features and units. *Geophysical Research Letters*, *41*, 8245–8251. https://doi.org/10.1002/2014GL062162

Le Feuvre, M., & Wieczorek, M. A. (2008). Nonuniform cratering of the terrestrial planets. *Icarus*, *197*, 291–306. https://doi.org/10.1016/j.icarus.2008.04.011

Le Feuvre, M., & Wieczorek, M. A. (2011). Nonuniform cratering of the Moon and a revised crater chronology of the inner solar system. *Icarus*, *214*, 1–20.

Manske, L., Marchi, S., & Wünnemann, K. (2019). Production and provenience of impact-generated melt by large scale collisions on Mars. 50th Lunar and Planetary Science Conference, #2753, The Woodlands, TX.

Marchi, S., Bottke, W. F., Kring, D. A., & Morbidelli, A. (2012). The onset of the lunar cataclysm as recorded in its ancient crater populations. *Earth and Planetary Science Letters*, *325–326*, 27–38.

Marchi, S., Chapman, C. R., Fassett, C. I., Head, J. W., Bottke, W. F., & Strom, R. G. (2013). Global resurfacing of Mercury 4.0–4.1 billion years ago by heavy bombardment and volcanism. *Nature*, *499*(7456), 59–61. https://doi.org/10.1038/nature12280

Marchi, S., Massironi, M., Cremonese, G., Martellato, E., Giacomini, L., & Prockter, L. (2011). The effects of the target material properties and layering on the crater chronology: The case of Raditladi and Rachmaninoff basins on Mercury. *Planetary and Space Science*, *59*, 1968–1980.

Meyer, J., Elkins-Tanton, L., & Wisdom, J. (2010). Coupled thermal–orbital evolution of the early Moon. *Icarus*, *208*, 1–10. https://doi.org/10.1016/j.icarus.2010.01.029

Michael, G. G. (2013). Planetary surface dating from crater size-frequency distribution measurements: Multiple resurfacing episodes and differential isochron fitting. *Icarus*, *226*, 885–890.

Michael, G. G., Kneissl, T., & Neesemann, A. (2016). Planetary surface dating from crater size-frequency distribution measurements: Poisson timing analysis. *Icarus*, *277*, 279–285.

Michael, G. G., & Neukum, G. (2010). Planetary surface dating from crater size-frequency distribution measurements: Partial resurfacing events and statistical age uncertainty. *Earth and Planetary Science Letters*, *294*, 223–229.

Miljković, K., Wieczorek, M. A., Collins, G. S., Laneuville, M., Neumann, G. A., Melosh, H. J., et al. (2013). Asymmetric distribution of lunar impact basins caused by variations in target properties. *Science*, *342*, 724–726.

Morbidelli, A., Marchi, S., Bottke, W. F., & Kring, D. A. (2012). A sawtooth-like timeline for the first billion years of lunar bombardment. *Earth and Planetary Science Letters*, *355–356*, 144–151.

Morbidelli, A., Nesvorny, D., Laurenz, V., Marchi, S., Rubie, D. C., Elkins-Tanton, L., et al. (2018). The timeline of the lunar bombardment: Revisited. *Icarus*, *305*, 262–276.

Neukum, G. (1971). *Untersuchungen tiber Einschlagskrater auf dem Mond.* Thesis: University of Heidelberg.

Neukum, G. (1977). Lunar cratering. *Philosophical Transactions of the Royal Society of London. Series A, Mathematical and Physical Sciences*, *285*, 267–272.

Neukum, G. (1983). *Meteoritenbombardement und datierung planetarer oberflaechen (Habilitation Thesis)* (pp. 1–186). München, Germany: Ludwig-Maximilians Universität München, Fakultät für Geowissenschaften.

Neukum, G., & Ivanov, B. A. (1994). Crater size distributions and impact probabilities on Earth from lunar, terrestrial planet, and asteroid cratering data. In T. Gehrels, M. S. Matthews, & A. M. Schumann (Eds.), *Hazards due to comets and asteroids* (pp. 359–416). Tucson: Univ. of Arizona Press.

Neukum, G., Oberst, J., Hoffmann, H., Wagner, R., & Ivanov, B. A. (2001). Geologic evolution and cratering history of Mercury. *Planetary and Space Science*, *49*, 1507–1521.

Neumann, G. A., Zuber, M. T., Wieczorek, M. A., Head, J. W., Baker, D. M., Solomon, S. C., et al. (2015). Lunar impact basins revealed by Gravity Recovery and Interior Laboratory measurements. *Science Advances*, *1*, e1500852.

Noyelles, B., Frouard, J., Makarov, V. V., & Efroimsky, M. (2014). Spin-orbit evolution of Mercury revisited. *Icarus*, *241*, 26–44.

Oberbeck, V. R., Quaide, W. L., Arvidson, R. E., & Aggarwall, H. R. (1977). Comparative studies of lunar, Martian, and Mercurian craters and plains. *Journal of Geophysical Research*, *82*, 1687–1698.

Orgel, C., Michael, G. G., Fassett, C. I., Van der Bogert, C. H., Riedel, C., Kneissl, T., & Hiesinger, H. (2018). Ancient bombardment of the inner solar system—Reinvestigation of the 'fingerprints' of different impactor populations on the lunar surface. *Journal of Geophysical Research: Planets*, *123*, 1–15. https://doi.org/10.1002/2017JE005451

Ostrach, L. R., Robinson, M. S., & Denevi, B. W. (2012). Distribution of impact melt on Mercury and the Moon. 43th Lunar and Planetary Science Conference, #1113, The Woodlands, TX.

Ostrach, L. R., Robinson, M. S., Whitten, J. L., Fassett, C. I., Strom, R. G., Head, J. W., & Solomon, S. C. (2015). Extent, age, and resurfacing history of the northern smooth plains on Mercury from MESSENGER observations. *Icarus*, *250*, 602–622.

Padovan, S., Wieczorek, M. A., Margot, J.-L., Tosi, N., & Solomon, S. C. (2015). Thickness of the crust of Mercury from geoid-to-topography ratios. *Geophysical Research Letters*, *42*, 1029–1038 https://doi.org/10.1002/2014GL062487

Pierazzo, E., Vickery, A. M., & Melosh, H. J. (1997). A reevaluation of impact melt production. *Icarus*, *127*, 408–423.

Povilaitis, R. Z., Robinson, M. S., Van de Bogert, C. H., Hiesinger, H., Meyer, H. M., & Ostrach, L. R. (2017). Crater density differences: Exploring regional resurfacing, secondary crater populations, and crater saturation equilibrium on the Moon. *Planetary and Space Science, xxx*, 1–11. https://doi.org/10.1016/j.pss.2017.05.006

Prockter, L. M., Ernst, C. M., Denevi, B. W., Chapman, C. R., Head, J. W., Fassett, C. I., et al. (2010). Evidence for young volcanism on Mercury from the third MESSENGER flyby. *Science*, *329*(5992), 668–671. https://doi.org/10.1126/science.1188186

Qingyun, D., Fei, L., Jianguo, Y., Zhiyong, X., & Rodriguez, J. A. P. (2018). Buried impact features on Mercury as revealed by gravity data. *Journal of Geophysical Research: Planets*, *123*, 3005–3019 https://doi.org/10.1029/2018JE005801

Riedel, C., Michael, G., Kneissl, T., Orgel, C., Hiesinger, H., & van der Bogert, C. H. (2018). A new tool to account for crater obliteration effects in crater size-frequency distribution measurements. *Earth and Space Science*, *5*, 258–267. https://doi.org/10.1002/2018EA000383

Roberts, J. H., & Barnouin, O. S. (2012). The effect of the Caloris impact on the mantle dynamics and volcanism on Mercury. *Journal of Geophysical Research*, *117*, E02007. https://doi.org/10.1029/2011JE003876

Robinson, M. S., Murchie, S. L., Blewett, D. T., Domingue, D. L., Hawkins, S. E., Head, J. W., et al. (2008). Reflectance and color variations on Mercury: Regolith processes and compositional heterogeneity. *Science*, *321*(5885), 66–69. https://doi.org/10.1126/science.1160080

Schmidt, R. M., & Housen, K. R. (1987). Some recent advances in the scaling of impact and explosion cratering. *International Journal of Impact Engineering*, *5*, 543–560.

Shearer, C. K., Hess, P. C., Wieczorek, M. A., Pritchard, M. E., Parmentier, E. M., Borg, L. E., et al. (2006). Thermal and magmatic evolution of the Moon. *Reviews in Mineralogy and Geochemistry*, *60*, 365–518.

Shoemaker, E. M. (1965). Preliminary analysis of the fine structure of the lunar surface in Mare Cognitum. *International Astronomical Union Colloquium*, *5*, 23–77.

Siegler, M. A., Bills, B. G., & Paige, D. A. (2013). Orbital eccentricity driven temperature variation at Mercury's poles. *Journal of Geophysical Research: Planets*, *118*, 930–937. https://doi.org/10.1002/jgre.20070

Spudis, P. D., & Guest, J. E. (1988). Stratigraphy and geologic history of Mercury. In F. Vilas, C. R. Chapman, & M. S. Matthews (Eds.), *Mercury* (pp. 118–164). Tucson: Univ. of Ariz. Press.

Stöffler, D., & Ryder, G. (2001). Stratigraphy and isotope ages of lunar geologic units: Chronological standard for the inner solar system. *Space Science Reviews*, *96*, 9–54.

Stöffler, D., Ryder, G., Ivanov, B. A., Artemieva, N. A., Cintala, M. J., & Grieve, R. A. (2006). Cratering history and lunar chronology. *Reviews in Mineralogy and Geochemistry*, *60*, 519–596.

Strom, R., Banks, M. E., Chapman, C. R., Fassett, C. I., Forde, J. A., Head, J. W., et al. (2011). Mercury crater statistics from MESSENGER flybys: Implications for stratigraphy and resurfacing history. *Planetary and Space Science*, *59*, 1960–1967.

Strom, R. G. (1977). Origin and relative age of lunar and Mercurian intercrater plains. *Physics of the Earth and Planetary Interiors*, *15*, 156–172.

Strom, R. G., Malhotra, R., Ito, T., Yoshida, F., & Kring, D. A. (2005). The origin of planetary impactors in the inner solar system. *Science*, *309*(5742), 1847–1850. https://doi.org/10.1126/science.1113544

Strom, R. G., Malhotra, R., Xiao, Z.-Y., Ito, T., Yoshida, F., & Ostrach, J. R. (2015). The inner solar system cratering record and the evolution of impactor populations. *Research in Astronomy and Astrophysics*, *15*(3), 407–434.

Strom, R. G., & Neukum, G. (1988). The cratering record on Mercury and the origin of impacting objects. In *Mercury* (pp. 336–373). Tucson: Univ. of Ariz. Press.

Strom, R. G., Trask, N. J., & Guest, H. E. (1975). Tectonism and volcanism on Mercury. *Journal of Geophysical Research*, *80*, 2478–2507.

Tanaka, K. L. (1982). A new time-saving crater-count technique, with application to narrow features. *NASA Technical Memorandum*, *TM-85127*, 123–125.

Tera, F., Papanastassiou, D. A., & Wasserburg, G. J. (1974). Isotopic evidence for a terminal lunar cataclysm. *Earth and Planetary Science Letters*, *22*, 1–21.

Thomas, R. J., Rothery, D. A., Conway, S. J., & Anand, M. (2014). Long-lived explosive volcanism on Mercury. *Geophysical Research Letters*, *41*, 6084–6092. https://doi.org/10.1002/2014GL061224

Tosi, N., Čadek, O., Běhounková, M., Káňová, M., Plesa, A.-C., Grott, M., & Wieczorek, M. A. (2015). Mercury's low-degree geoid and topography controlled by insolation-driven elastic deformation. *Geophysical Research Letters*, *42*, 7327–7335. https://doi.org/10.1002/2015GL065314

Trask, N. J., & Guest, J. E. (1975). Preliminary geologic terrain map of Mercury. *Journal of Geophysical Research*, *80*, 2461–2477. https://doi.org/10.1029/JB080i017p02461

Vander Kaaden, K. E., & McCubbin, F. M. (2015). Exotic crust formation on Mercury: Consequences of shallow, FeO-poor mantle. *Journal of Geophysical Research*, *120*, 195–209. https://doi.org/10.1002/2014JE004733

Vasavada, A. R., Paige, D. A., & Wood, S. E. (1999). Near-surface temperatures on Mercury and the Moon and the stability of polar ice deposits. *Icarus*, *141*, 179–193.

Bottke, W. F., Vokrouhlický, D., Minton, D., Nesvorný, D., Morbidelli, A., Brasser, R., et al. (2012). An Archaean heavy bombardment from a destabilized extension of the asteroid belt. *Nature*, *485*, 78–81.

Watters, T. R., Head, J. W., Solomon, S. C., Robinson, M. S., Chapman, C. R., Denevi, B. W., et al. (2009). Evolution of the Rembrandt impact basin on Mercury. *Science*, *324*(5927), 618–621. https://doi.org/10.1126/science.1172109

Weider, S. Z., Nittler, L. R., Starr, R. D., Crapster-Pregont, E. J., Peplowski, P. N., Denevi, B. W., et al. (2015). Evidence for geochemical terranes on Mercury: Global mapping of major elements with MESSENGER's X-Ray Spectrometer. *Earth and Planetary Science Letters*, *416*, 109–120.

Werner, S. C. (2014). Moon, Mars, Mercury: Basin formation ages and implications for the maximum surface age and the migration of gaseous planets. *Earth and Planetary Science Letters*, *400*, 54–65.

Whitten, J. L., & Head, J. W. (2015). Rembrandt impact basin: Distinguishing between volcanic and impact-produced plains on Mercury. *Icarus*, *258*, 350–365.

Whitten, J. L., Head, J. W., Denevi, B. W., & Solomon, S. C. (2014). Intercrater plains on Mercury: Insights into unit definition, characterization, and origin from MESSENGER datasets. *Icarus*, *241*, 97–113.

Wichman, R. W., & Schultz, P. H. (1989). Sequence and mechanisms of deformation around the Hellas and Isidis impact basins on Mars. *Journal of Geophysical Research*, *94*, 17,333–17,357.

Wieczorek, M. A., Correia, A. C. M., Le Feuvre, M., Laskar, J., & Rambaux, N. (2012). Mercury's spin-orbit resonance explained by initial retrograde and subsequent synchronous rotation. *Nature Geoscience*, *5*, 18–21.

Wilhelms, D. E. (1976). Mercurian volcanism questioned. *Icarus*, *28*, 551–558.

Williams, J.-P., Ruiz, J., Rosenburg, M. A., Aharonson, O., & Phillips, R. J. (2011). Insolation driven variations of Mercury's lithospheric strength. *Journal of Geophysical Research*, *116*, E01008. https://doi.org/10.1029/2010JE003655

Woronow, A. (1977). Crater saturation and equilibrium: A Monte Carlo simulation. *Journal of Geophysical Research*, *82*(17), 2447–2456.

Xiao, Z., Werner, S. C. (2015). Size-frequency distribution of crater populations in equilibrium on the Moon. *Journal of Geophysical Research: Planets*, *120*, 2277–2292. https://doi.org/10.1002/2015JE004860

Zellner, N. E. B. (2017). Cataclysm no more: New views on the timing and delivery of lunar impactors. *Astrobiology*, *47*(3), 261–280. https://doi.org/10.1007/s11084-017-9536-3